JACS
JOURNAL OF THE AMERICAN CHEMICAL SOCIETY

Article

pubs.acs.org/JACS

Design, Synthesis, and Dynamics of a Green Fluorescent Protein Fluorophore Mimic with an Ultrafast Switching Function

Marco Paolino,[*,†] Moussa Gueye,[‡] Elisa Pieri,[†,¶] Madushanka Manathunga,[§,¶] Stefania Fusi,[†] Andrea Cappelli,[†] Loredana Latterini,[∥] Danilo Pannacci,[∥] Michael Filatov,[*,⊥] Jérémie Léonard,[*,‡] and Massimo Olivucci[*,†,§,#]

[†]Dipartimento di Biotecnologie, Chimica e Farmacia, Università di Siena, Via A. Moro 2, 53100 Siena, Italy

[‡]Institut de Physique et Chimie des Matériaux de Strasbourg & Labex NIE, Université de Strasbourg, CNRS UMR 7504, Strasbourg, France

[§]Chemistry Department, Bowling Green State University, Bowling Green, Ohio, United States

[∥]Dipartimento di Chimica, Biologia e Biotecnologie, Università di Perugia, Via Elce di Sotto, 8, 06123 Perugia, Italy

[⊥]Department of Chemistry, School of Natural Sciences, Ulsan National Institute of Science and Technology (UNIST), Ulsan 689-798, Korea

[#]University of Strasbourg Institute for Advanced Studies, 5, allée du Général Rouvillois F-67083 Strasbourg, France

Supporting Information

ABSTRACT: While rotary molecular switches based on neutral and *cationic* organic π-systems have been reported, structurally homologous *anionic* switches providing complementary properties have not been prepared so far. Here we report the design and preparation of a molecular switch mimicking the anionic *p*-HBDI chromophore of the green fluorescent protein. The investigation of the mechanism and dynamics of the *E*/*Z* switching function is carried out both computationally and experimentally. The data consistently support axial rotary motion occurring on a sub-picosecond time scale. Transient spectroscopy and trajectory simulations show that the nonadiabatic decay process occurs in the vicinity of a conical intersection (CI*nt*) between a charge transfer state and a covalent/diradical state. Comparison of our anionic *p*-HBDI-like switch with the previously reported cationic *N*-alkyl indanylidene pyrrolinium switch mimicking visual pigments reveals that these similar systems translocate, upon vertical excitation, a similar net charge in the same axial direction.

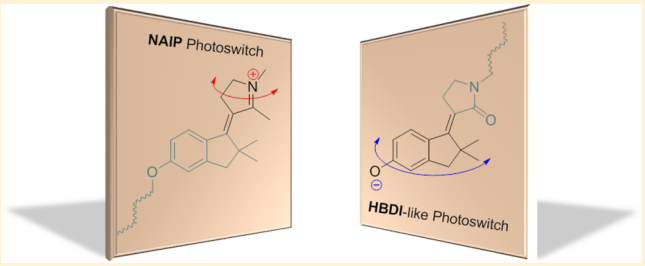

INTRODUCTION

The conversion of light energy into molecular motion is at the basis of the development of light-driven molecular devices such as molecular switches and motors.[1,2] Among these systems, single-molecule rotary devices are capable of funneling the energy of a photon into double bond isomerization modes and setting a *rotor* moiety in motion with respect to a *stator* framework.[3] Such a functionality has been employed in a number of prototype applications showing that it is possible to control ion complexation,[4,5] catalysis,[6] folding/unfolding of oligopeptides,[7] and other properties.[8−11]

While most of the above applications employed unnatural chromophores such as azobenzene, stilbene, and imine derivatives, during the past years, we have shown that mimicking closely the photoisomerization of biological chromophores represents a viable strategy for achieving alternative light-driven rotary devices. Indeed, we have reported the synthesis of several positively charged N-alkylated or N-protonated indanylidene pyrroline Schiff bases (NAIPs and NHIPs, respectively).[12−18] These (see Scheme 1, left) are biomimetic structures which replicate the reactivity of the retinal chromophore of visual pigments. For instance, NAIPs (in the following, we use NAIP to refer, in general terms, to both NAIP

Scheme 1. Molecular Framework of the Cationic Retinal Protonated Schiff Base Mimics MeO-NAIP (R = R′ = CH_3) and MeO-NHIP (R = H, R′ = CH_3) Compared with the Molecular Framework of the GFP Fluorophore *p*-HBDI Anion[a]

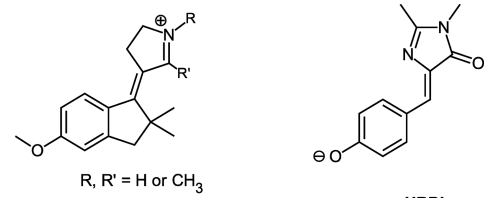

[a]The moiety of dMe-MeO-NAIP with R = CH_3, R′ = H is also discussed in the next sections.

Received: October 21, 2015
Published: June 20, 2016

DOI: 10.1021/jacs.5b10812
J. Am. Chem. Soc. 2016, 138, 9807−9825

and NHIP) have been shown to undergo a regioselective subpicosecond double bond photoisomerization similar to that observed for the protein embedded chromophore of animal and microbial rhodopsins.[13,14,16,17] Due to their cationic nature, NAIPs provide opportunities for achieving systems with repositioning or rotating positively charged rotors with promising applications in materials science, synthetic biology, and nanotechnology.[19,20]

In spite of the results described above, it was not obvious until now that a biomimetic strategy could be successfully employed for achieving rotary devices beyond the current biological mimics. In the present report, we show that this is indeed the case by preparing a novel light driven switch bearing a negatively charged, rather than neutral or positively charged, rotor. More specifically, our biomimetic strategy has been reemployed to design and prepare a molecular switch mimicking the radiationless photoisomerization of the green fluorescent protein (GFP) fluorophore: the *para*-4-hydroxybenzylidene-2,3-dimethylimidazolinone (*p*-HBDI) anion (see Scheme 1, right).

GFP, originally from the jellyfish *Aequorea victoria*, can be readily expressed in a range of other organisms from microbes to mammals,[21] and it is widely used as a genetically encodable fluorescent probe due to its high fluorescence quantum yield, relatively small size, and spectroscopic features which can be tuned via mutation.[22] The *p*-HBDI fluorophore of GFP is hosted in a tight β-barrel cavity, which locks its central double bond and the adjacent single bond, yielding a photochemically nonreactive molecule and, consequently, an efficient emitter.[21,23,24] This conclusion is supported by the extreme loss of fluorescence displayed by *p*-HBDI in solution.[25] In fact, it has been shown both computationally[26] and experimentally[27] (both in isolated conditions[28] and in solution[29]) that a rapid twisting of the *p*-HBDI central bond[30] leads to radiationless deactivation via decay at a conical intersection between the first singlet excited state (S_1) and the ground state (S_0) of the molecule.[31]

The behavior described above has prompted us to look for *p*-HBDI mimics which could undergo the type of regioselective double bond isomerization required for the construction of rotary switches and motors but that, at the same time, could be efficiently prepared. Accordingly, we report on the computational design, preparation, and spectroscopic characterization of a synthetic *p*-HBDI mimic featuring a single exocyclic and photoisomerizable double bond connecting two rigid units. We show that the new switch not only offers features complementary to NAIPs (e.g., it is *negatively* rather than *positively* charged) but can also be prepared more efficiently, which is highly beneficial for its future applications.

RESULTS AND DISCUSSION

Design and Modeling. Only few studies pointed to the development of molecular switching functions based on *p*-HBDI mimics. Specific mutations of GFP or GFP-like proteins yielded chromophores capable of undergoing *E*/*Z* isomerization, making the protein fluorescence switchable via irradiation at specific wavelengths.[32] A synthetic *p*-HBDI mimicking switch has been proposed by Sampedro and co-workers;[33,34] however, its rotor is conformationally flexible due to the conservation of the exocyclic single bond present in the native *p*-HBDI framework (see Scheme 1) and does not contain the phenolic group needed to generate the corresponding anion. In order to design a *p*-HBDI-like framework with locked stator and rotor orientations, we decided to restrain the *p*-HBDI aromatic ring twisting by adding an ethylene ($-CH_2-CH_2-$) bridge to the structure (compare left and right structures in Figure 1). The bridge would prevent dissipation of the absorbed photon energy through rotation about the single aryl−alkene bond. We also decided to replace the imidazolone with a pyrrolidone moiety mainly to enable a facile synthesis (as detailed below) but also to enhance the translocation of the indanylidene negative charge along the molecular framework upon light absorption. This would facilitate the S_1 isomerization (i.e., the spectroscopic state S_1 is expected to have charge transfer character and its electronic structure is dominated by the resonance formula at the bottom right of Figure 1).

Before describing the synthesis and kinetic characterization (next subsection) of the anionic *p*-HBDI-like switch (from now on, "*p*-HBDI-like" will refer exclusively to the anionic form), it is useful to analyze its intrinsic (i.e., gas-phase) spectroscopy and reactivity computationally. Since the switch is designed to work

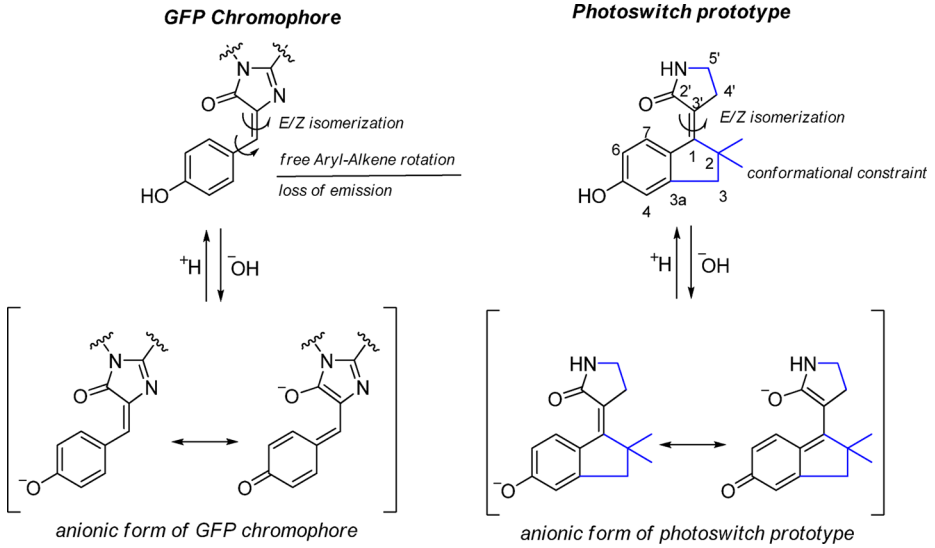

Figure 1. Structure of GFP chromophore (left), whose fluorescent anionic form corresponds to an alkyl derivative of *p*-HBDI, compared with the structure of the *Z* isomer of our designed *p*-HBDI-like switch (right). Both the neutral and anionic forms are displayed. The bonds in blue represent the points of modification with respect to the native *p*-HBDI structure.

DOI: 10.1021/jacs.5b10812
J. Am. Chem. Soc. 2016, 138, 9807−9825

in a polar solution environment, we do not deal here with the possibility of spontaneous electron detachment which may compete with the production of a bound excited state when an anion is in isolated conditions.[35,36] Accordingly, the *p*-HBDI-like S_0 and S_1 potential energy surfaces (PESs) were mapped both via density functional theory computations employing the REKS and SI-SA-REKS methods[37] and via wave function based computations employing the CASPT2//CASSCF protocol (see the Materials and Methods section for details). The S_0 equilibrium structures of the *E* and *Z* isomers of the switch are found to exist in conformations with P and M helicities and pyramidalized nitrogens, yielding two pairs of enantiomers (i.e., the P,R and M,S pair and the M,R and P,S pair) in a diastereomeric relationship with each other. Figure 2 displays the detailed *E*-P,R

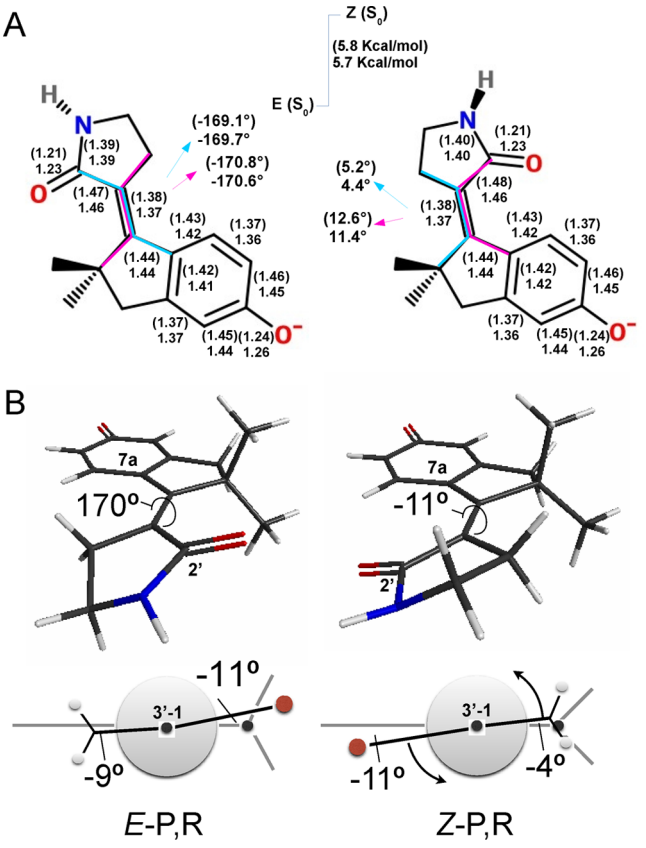

Figure 2. Computed gas-phase S_0 equilibrium structures of the designed *p*-HBDI-like switch. (A) Comparison between the relative energy and main geometrical parameters computed at the REKS and CASSCF (in parentheses) levels for the *E* (left) and *Z* (right) isomers in the P,R configuration: both computational methods yield similar results. (B) Perspective representation and Newman projections of the same *E*-P,R and *Z*-P,R structures.

and *Z*-P,R diastereoisomers featuring P helicity and a R configuration of the nitrogen. As changing the N configuration did not seem to be relevant for studying the double bond isomerization, the N-inversion process was not investigated.

Figure 3 reports the energies of the located minima and transition states along schematic S_0 and S_1 REKS energy profiles as a function of the C2′−C3′−C1−C7a dihedral angle (see Figure 1 for the numbering) describing the progression along the reaction coordinate. On the S_0 PES, the *E*-P,R stereoisomer, which is found to be the lowest in energy, does not feature a stable M,R diastereoisomer possibly because inversion of the pyrrolidone ring with R nitrogen disfavors the M helicity. However, both *Z*-P,R and *Z*-M,R could be located with the former lying 6.0 kcal/mol above *E*-P,R and the latter being 2.1 kcal/mol less stable. These diastereoisomers are connected by a shallow transition state with an activation barrier of 1.8 kcal/mol controlling the conversion from M to P leading to a change in helicity.

As shown in Figure 3, when starting from *E*-P,R, the thermal $E \rightarrow Z$ isomerization would directly produce the *Z*-M,R diastereomer by overcoming a large barrier. *Z*-M,R is then converted to *Z*-P,R via a shallow but distinct transition state. On the other hand, *Z*-P,R is connected to the original *E*-P,R structure through a second high energy transition state located 26.8 kcal/mol higher. If the ca. 30 kcal/mol computed $E \rightarrow Z$ and $Z \rightarrow E$ activation barriers are conserved in solution, one would predict a very slow thermal isomerization at room temperature with the system reaching the thermal equilibrium only at higher temperatures.

The vertical excitation energies calculated for the most stable *E*-P,R and *Z*-P,R *p*-HBDI-like diastereomers were obtained using the SSR-LC-ωPBE/6-31+G* method (see the Materials and Methods section for details). As shown in Figure 3, these correspond to 347 nm for *E*-P,R and 368 nm for *Z*-P,R, respectively. The difference between these values is suitable for modulating the photostationary state composition if, again, such a difference is maintained in solution. Using the SSR-LC-ωPBE/6-31+G* method, we located two minimum energy conical intersections (MECIs), which correspond to real crossings between the S_1 and S_0 PESs. These MECIs lie below the FC points by 18.9 kcal/mol ($MECI_{270}$ connecting *E*-P,R to *Z*-M,R) and 19.6 kcal/mol ($MECI_{90}$, connecting *Z*-P,R to *E*-P,R). The MECI geometries are shown in Figure 4A along with the corresponding branching plane (BP) vectors.

As apparent from Figure 3, the S_1 PES near the *E*-P,R and *Z*-P,R Franck−Condon (FC) points is rugged but flat (with energy barriers below 2.3 kcal/mol). The energy profile shows only a modest initial relaxation along the bond length alternation (BLA) displacement inverting skeletal double and single bonds (the BLA value is calculated as the difference between the average length of the single bonds and the average length of the double bonds in the O═C2′—C3′═C1—C7a═C7—C6═C5—O framework). In contrast, along the reactive double bond twisting coordinate (described by the C2′—C3′—C1—C7a dihedral angle), the flatness of the PES implies a nearly barrierless double bond twist. However, beyond ca. 40° twisting, the energy decreases sharply and distinct S_1 energy minima (not shown in Figure 3) are reached at ca. 90° twisting. These minima are only slightly (ca. 1 kcal/mol) below the corresponding MECIs, suggesting rapid decay to S_0 in spite of the weakly sloped rather than peaked topography[38] of the located MECIs. Such topography will be further discussed below.

It is noteworthy that the *E*-P,R conformation is pretwisted through ca. 10° in the counterclockwise (CCW) sense. This suggests that reaching $MECI_{270}$ from the *E*-P,R FC point is expected to be preferred, which implies a preference for CCW twisting. However, the flatness of the S_1 PES makes this prediction uncertain and dynamic simulations are needed to prove this conjecture. The same conjecture applies to *Z*-P,R that also features a CCW pretwisted structure prompting the isomerization motion toward $MECI_{90}$. Of course, a preferential CCW twisting of both *E*-P,R and *Z*-P,R would accomplish a complete $E \rightarrow Z \rightarrow E$ rotation relative to the *E*-P,R isomer fueled by the sequential absorption of two photons. Symmetry considerations lead to the conclusion that the *E*-M,S enantiomer of *E*-P,R would undergo a complete rotation in the opposite CW direction.

DOI: 10.1021/jacs.5b10812
J. Am. Chem. Soc. 2016, 138, 9807−9825

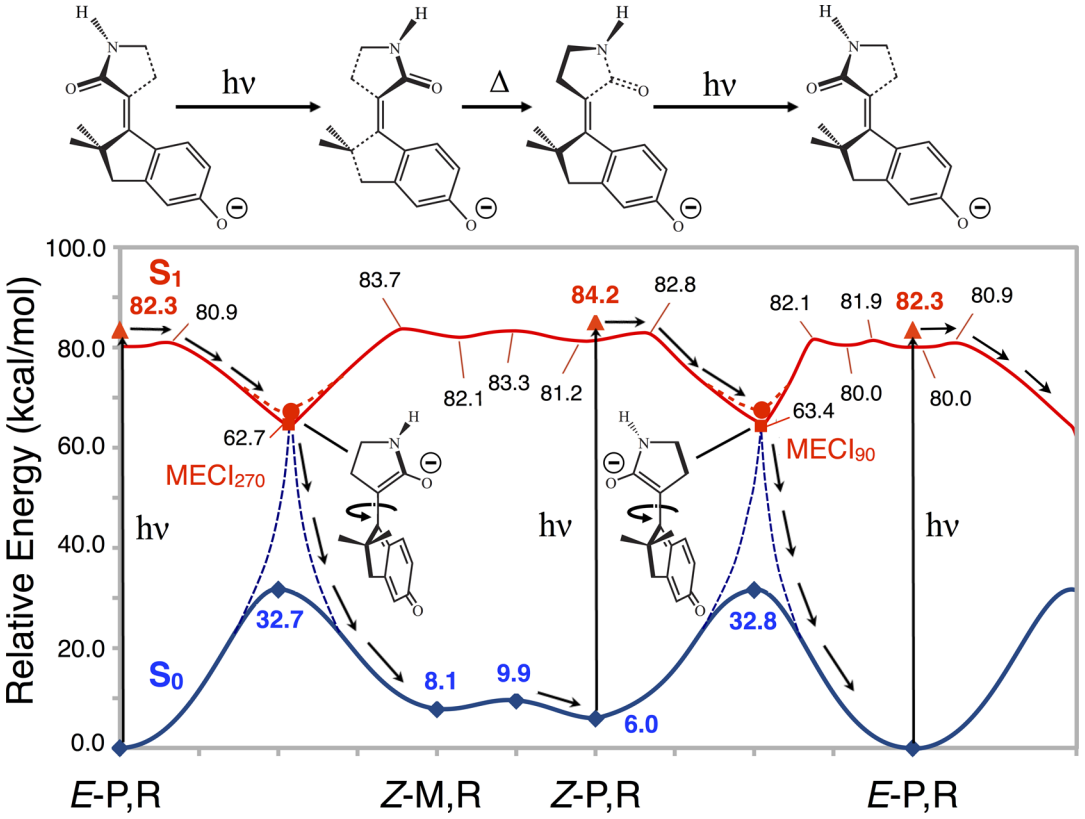

Figure 3. Schematic S_0 (blue) and S_1 (red) energy profiles along the isomerization paths of the *p*-HBDI-like switch. The reaction coordinate describes the counterclockwise twisting of the pyrrolidone moiety with respect to the indanylidene moiety, and the stream of arrows illustrates two sequential photochemical isomerization events. The energy profiles are computed at the SI-SA-REKS level of theory. The S_0 stationary points are shown as blue diamonds. The red triangles mark the vertical excitations at the optimized *E*-P,R and *Z*-P,R S_0 structures (i.e., the Franck−Condon points). The equilibrium S_1 minima are represented by red squares. The optimized MECIs where S_0 and S_1 energies are degenerate are marked with red circles. The energy profiles describing the relaxation paths through the MECI points along S_1 and S_0 are pictorially represented by dashed lines.

For a reaction occurring through a CI*nt*, the BP vectors play a role similar to the transition vector at a transition state driving a thermal reaction.[38,39] Thus, the BP analysis provides information on the atomic displacements leading away from the nonadiabatic coupling (i.e., from the MECI structures or from other nearby intersection seams and avoided crossing points) and, in turn, on the isomerization mechanism.[40−42] The BP vectors of the two MECIs of the *p*-HBDI-like switch are found to correspond, roughly, to the twisting about the exocyclic double bond and to the BLA mode (X_1 and X_2 in Figure 4A, respectively). Interestingly, these are the same BP displacements documented for NAIP molecular switches.[42] Such a similarity is consistent with a recent study[42] showing that switches undergoing a predominantly heterolytic breaking of a π-bond are likely to have S_1/S_0 MECI characterized by a twisting/BLA BP as opposed to the twisting/pyramidalization BP typical of molecules undergoing a predominantly homolytic π-bond breaking (e.g., polyenes). Indeed, the two electronic configurations representing the intersecting S_0 and S_1 states of the designed switch have charge-transfer (CT) closed-shell character and diradical (DIR) open-shell character, respectively (see Figure 4B). As we will now discuss, these electronic structures play an important role in determining the reactivity and S_1 dynamics of the system.

To test the possible involvement of triplet states in the switch photoisomerization, we have searched for minimum energy crossing points (MECPs) between the ground triplet state (T_0) and the S_0 and S_1 states. No T_0/S_1 MECP could be located within the energy range covered in Figure 3. Two T_0/S_0 MECPs were instead located in the proximity of each S_1/S_0 MECI point. Although these MECPs lie within 3 kcal/mol and are geometrically (RMSD ca. 0.034−0.036 Å) close to the MECIs, the S_1-S_0 energy gap at the position of these MECPs is in the range of 13 kcal/mol. Taken together, these results suggest that the T_0 population is not likely within the energy range achieved in the experiments, and that $S_1 \rightarrow S_0 \rightarrow T_0$ is unfeasible due to the wide S_1-S_0 energy gap at MECPs.

The SI-SA-REKS computations above provide reliable information on the PES structure of the bound S_1 state driving the switch photoisomerization.[43] However, the simulation of the dynamics of nonadiabatic processes at the SI-SA-REKS level is still impractical. For this reason, the gas-phase S_1 evolution and lifetime of the *p*-HBDI-like switch have been investigated using scaled-CASSCF semiclassical trajectories.[44] These are single surface-hop trajectories released from the FC point with no initial kinetic energy (from now on called FC trajectories) and employed for mechanistic studies of events falling in the sub-picosecond regime. Generally, there is a good agreement between the geometries, relative energies, and charge distributions of the species calculated by the SI-SA-REKS and the scaled-CASSCF methods (see the Supporting Information for more detail); hence, the latter method can be used in lieu of the former in the dynamics simulations.

The comparison of the S_0 equilibrium structures computed at the CASSCF and SI-SA-REKS levels (see Figure 2) and the comparison of the structures of the minima located along the flat CASPT2//CASSCF minimum energy path (MEP) S_1 energy

DOI: 10.1021/jacs.5b10812
J. Am. Chem. Soc. 2016, 138, 9807−9825

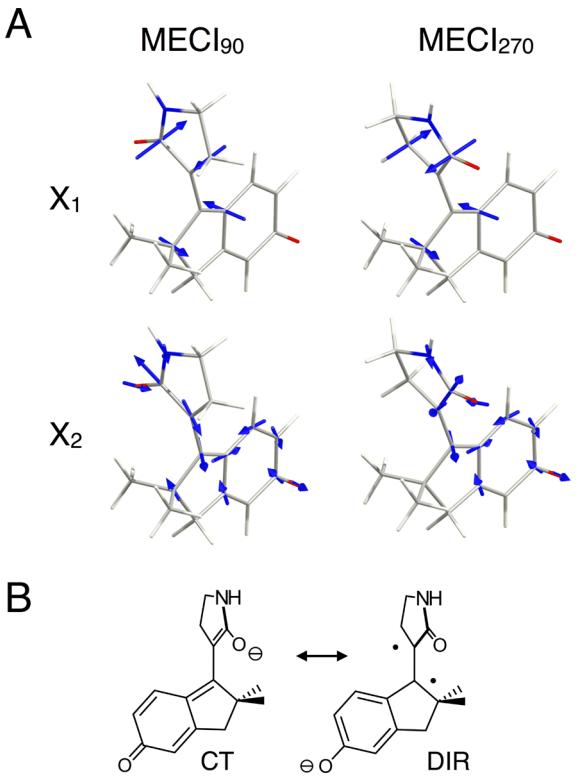

Figure 4. MECIs of the *p*-HBDI-like switch. (A) Geometries of the switch at the intersection connecting the *E*-P,R and *Z*-M,R stereoisomers (left) and the intersection connecting *Z*-P,R to *E*-P,R stereoisomers (right). The blue arrows, representing the atomic displacements in the BP vectors of both structures, correspond to double bond twisting (X_1) and BLA (X_2) distortions. (B) Lewis resonance structures dominating the intersecting S_0 and S_1 wave functions at the MECIs.

profiles (see Figure 5A and B) and the corresponding SI-SA-REKS S_1 minima of Figure 3 indicate a structural consistency between the two levels of theory. The energy difference between the equilibrium *E*-P,R and *Z*-P,R forms is also consistent (6.0 and 6.1 kcal/mol at the SI-SA-REKS and CASPT2//CASSCF levels, respectively), as it is for the charge distribution (see Table 1) for the FC structures and structures closest to the MECIs (indicated as "AC" in both Figure 5 and Table 1). On the other hand, the CASPT2//CASSCF excitation energies appear ca. 5 and 7 kcal/mol red-shifted with respect to the SI-SA-REKS values when using the 6-31G* and 6-31+G* basis sets, respectively, although all levels of theory consistently predict that the λ_{max} of *E*-P,R is blue-shifted compared to that of *Z*-P,R (see also the next subsection). Such excitation energy differences are assumed not to affect significantly the mechanistic information provided by the *E*-P,R and *Z*-P,R FC trajectories of Figure 5C.

It is apparent that, consistently with the MEP results of Figure 5A, the initial S_1 dynamics of the *p*-HBDI-like switch is, in general, dominated by a stretching relaxation (this is described by the bond length *L* defined in Figure 5C) followed by the central bond twisting relaxation along a flat S_1 potential energy region. Progression along a twisting (i.e., isomerization) coordinate is best reflected by the evolution of the value of the τ angle (the τ angle defined in Figure 5B reflects, approximately, the magnitude of the overlap between the π-systems of the indanylidene and pyrrolidone units) rather than the C2′−C3′−C1−C7a dihedral, and it confirms that, for the specific case of the *E*-P,R and *Z*-P,R diastereomers, the rotation proceeds in a CCW direction. Both diastereomers then reach an avoided crossing (AC) region in ca. 500 fs and continue their S_1 motion without decay to S_0. This suggests that a sub-picosecond decay may occur either via vibrational excitation or, as we will show below, via a solvent effect changing the topology of the PES in the decay region (e.g., changing an AC into a CI*nt* point). Indeed, as we will document below, an AC region is also detected in the gas-phase FC trajectory of the homologue MeO-NHIP switch of Scheme 1, while the corresponding condensed-phase FC trajectories (i.e.,, in a box of explicit MeOH solvent molecules) have been shown to intercept a region with much smaller S_1−S_0 energy gap, directly at a CI*nt* point, on a shorter time scale.[13]

A different property of the computed S_1 trajectories is revealed by the analysis of the charge translocation along the switch backbone. This analysis reflects the character of the S_1 electronic structure (i.e., the electronic wave function) in terms of the weight of CT or DIR resonance Lewis structure/electronic configuration (see Figure 4B). As displayed in Table 1, it turns out that (i) at the S_0 equilibrium structure (FC) the character of the S_0 wave function is mixed but dominated by the DIR/COV character (COV stands for covalent; DIR/COV indicates that the COV character smoothly turns into a DIR character at highly twisted double bond geometries where a homolytic π-bond breaking is accomplished); (ii) at the same FC structure the character of the S_1 wave function is mixed and contains both CT and DIR characters; (iii) after ca. 400 fs dynamics and in a situation where the twisting double bond is ca. 40° twisted, the S_1 electronic configuration dominating the reacting system turns to be completely DIR. Point iii indicates that the system is moving along a region of the S_1 PES which better correlates with the S_0, rather than S_1 wave function at the reactant structure. As we will detail in a comparative analysis below, such a region also appears in the MeO-NHIP switches but closer to the AC point, while a modestly dominating CT character is maintained along the twisting.

By definition, the CT and DIR character of the S_1 wave function are interchanged at a CI*nt* point.[45] Therefore, in order to provide an explanation for the fact that the *p*-HBDI-like switch intercepts an AC rather than a CI*nt* and for the fact that a large region of the S_1 PES has an electronic structure dominated by a DIR character, we have explored the MECI topography. As shown in Figure 6, it is found, at all levels of theory and for both the $MECI_{90°}$ and $MECI_{270°}$, that the intersection does not display a peaked topography but a slightly sloped topography along the X_2 vector dominated by the BLA coordinate. The S_1 energy profile correctly displays, for both *E*-P,R and *Z*-P,R, a minimum located slightly lower than the MECI point, as also found via geometry optimization (see above). Such a minimum has an electronic structure corresponding to the DIR character. The stationary point energies of Figure 3, the energy profiles of Figure 5A and C, and the energy profiles along X_2 in Figure 6A converge in the schematic representation of Figure 6B which summarizes the computational characterization of the designed molecule as well as the possible S_1 evolution.

Synthesis and Photochemistry. The designed *p*-HBDI-like switch was synthesized starting from 5-methoxy-1-indanone. Following the synthetic route shown in Scheme 2, the starting material was bismethylated in position C2 to obtain the indanone **1** which was then reacted with *N*-Boc-pyrrolidinone to obtain **2** through dehydration of the aldol condensation intermediate. The bis methyl substitution on the C2 of the 5-methoxy-1-indanone was performed to prevent the possible competition between the *endo* and *exo* cyclic dehydration of the intermediate alcohol.

DOI: 10.1021/jacs.5b10812
J. Am. Chem. Soc. 2016, 138, 9807−9825

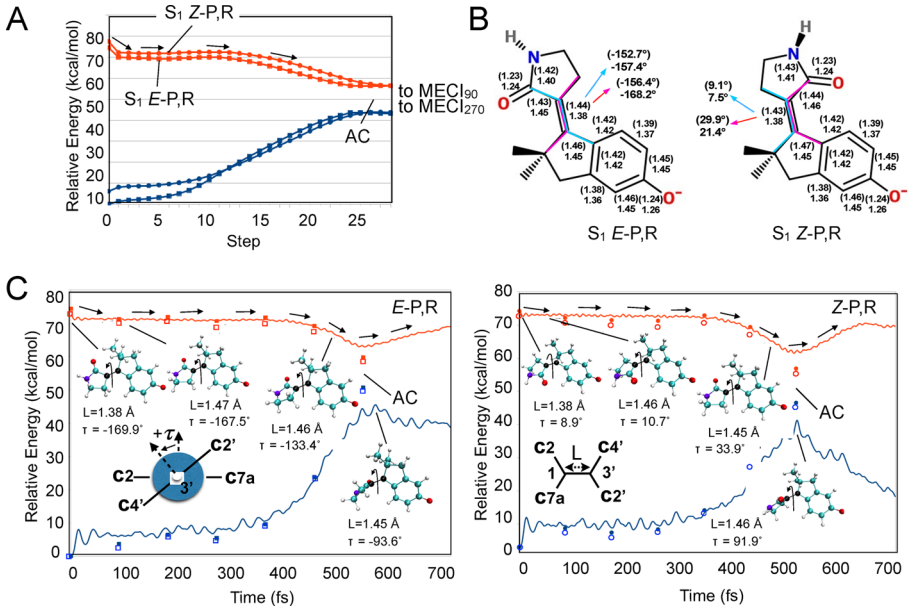

Figure 5. S_1 evolution of the *p*-HBDI-like switch. (A) S_1 (red) and S_0 (blue) energy profiles computed along the MEP (CASPT2//CASSCF/6-31G* level with a radius of 0.07 Å·(amu)$^{1/2}$) starting from both the *E*-P,R (circles) and *Z*-P,R (square) FC points and leading to the $MECI_{270}$ and $MECI_{90}$, respectively (see Figure 3). (B) Comparison between the located SI-SA-REKS *E*-P,R and *Z*-P,R S_1 energy minima of Figure 3 and the structures located at the center of the two S_1 shallow valleys found along the *E*-P,R and *Z*-P,R MEPs. The values in parentheses (Å and deg) refer to the CASSCF geometry. (C) Scaled-CASSCF/6-31G* S_1 FC trajectories for *E*-P,R and *Z*-P,R. The full circles and full squares refer to the single point CASPT2/6-31G* computations performed along the unscaled-CASSCF trajectories and used for scaling the CASSCF energy gaps and time scales (see the Supporting Information for details) given by the full lines. The corresponding open square points refer to the 6-31+G* basis set which does not seem to have a significant effect on the energy profile in spite of the additional diffuse functions. This is more probably due to the rather delocalized nature of the anionic charge. The structures along the trajectories provide information on the main geometrical evolution of the isomers (parameters in Å and deg). The definitions of the angle τ and bond length L are given as insets.

Table 1. Charge Evolution along the Trajectories of Figure 5C[a]

	E-P,R charges		*Z*-P,R charges	
	indanylidene frag.[b]	pyrrolidone frag.[b]	indanylidene frag.[b]	pyrrolidone frag.[b]
S_0 FC	−0.62 (−0.56)	−0.38 (−0.44)	−0.61 (−0.58)	−0.39 (−0.42)
S_1 FC	−0.51 (−0.58)	−0.49 (−0.42)	−0.51 (−0.58)	−0.49 (−0.42)
S_1 90 fs	−0.50	−0.50	−0.49	−0.51
S_1 180 fs	−0.52	−0.48	−0.50	−0.50
S_1 270 fs	−0.51	−0.49	−0.50	−0.50
S_1 360 fs	−0.56	−0.44	−0.56	−0.44
S_1 450 fs	−0.73	−0.27	−0.71	−0.29
S_1 AC	−0.98 [−0.96]	−0.02 [−0.04]	−0.98	−0.02
S_0 360 fs	−0.50	−0.50		
S_0 450 fs	−0.31	−0.69		
S_0 AC	−0.07 [−0.05]	−0.93 [−0.95]		

[a]We set the CT character dominating when the indanylidene fragment has charge ≥ −0.5 and the COV/DIR character dominating when the indanylidene fragment has charge < −0.5. [b]Numbers in parentheses indicate the corresponding values for the REKS optimized structures, and those in the square brackets, the values corresponding to the optimized MECIs (see Figure 3).

The methoxy group of **2** was then deprotected with BBr_3 to get the final phenolic compound **3** as an *E*/*Z* mixture (8:2). In compound **3**, the phenolic group is placed in the *para* position with respect to the double bond similarly to *p*-HBDI fluorophore, while carbons C2 and C3 (see Figure 1 for the numbering) provide the conformational locking of the final molecule. In conclusion, **3** was prepared in only three steps (compared to six required for the synthesis of the homologue NAIP compound in Scheme 2) and a total yield of 58% (versus ∼43% for the NAIP).[46,14]

Compounds **2** and **3** have been characterized by homonuclear and heteronuclear NMR analysis. In particular, NOE experiments on both compounds evidence contacts between H-4′ and H-7 for a dominant form and between H-4′ and H-A for a minor form, attributed to *E* and *Z* configurations, respectively. Moreover, the chemical structures and the configurations of *E*-**2** and *E*-**3** were also confirmed by crystallography and reported in Figures S1 and S2 of the Supporting Information.

The absorption spectrum of *E*-**3** depends significantly on the pH and the solvent.[47] The absorption maxima (λ_{max}) and spectra of **3** in different solvents and at neutral or strongly basic pH (i.e., after adding an excess of KOH to generate the target anionic form of the phenol) are reported in Table 2 and Figure 7. The neutral form of the *E*-**3** and *Z*-**3** isomers does not display significant solvatochromism, with λ_{max} values remaining in the 318−320 and 319−324 nm ranges, respectively. By contrast, the anion corresponding to the designed *p*-HBDI-like switch not

DOI: 10.1021/jacs.5b10812
J. Am. Chem. Soc. 2016, 138, 9807−9825

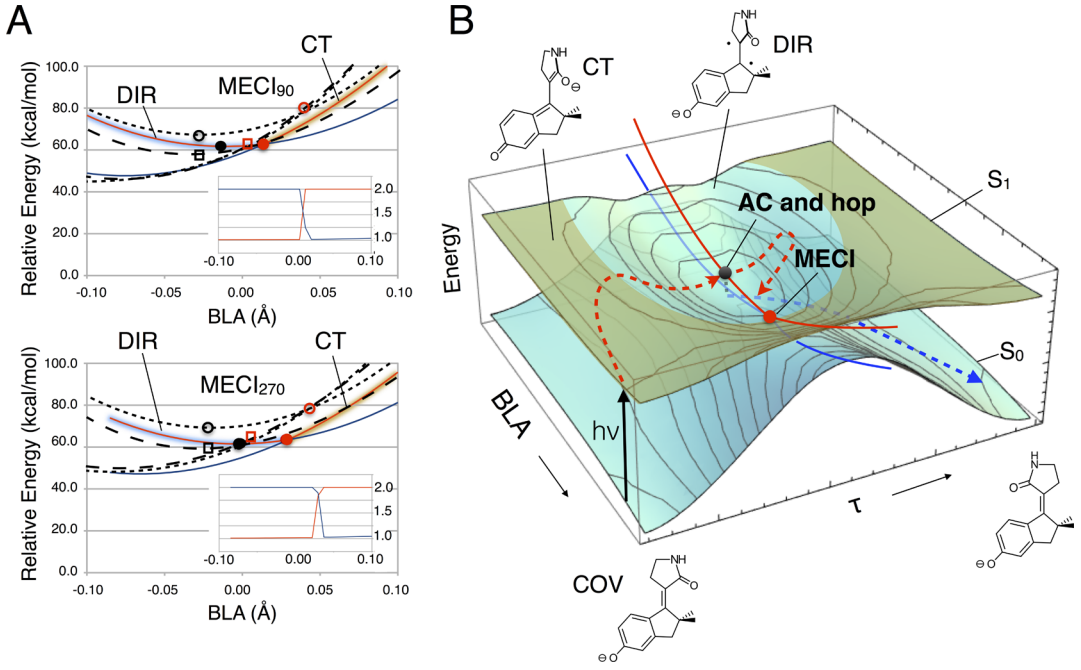

Figure 6. Structure of the PES driving *p*-HBDI-like photoisomerizations. (A) S_0 and S_1 energy profiles along cross sections corresponding to the X_2 vector of Figure 4A for the located MECIs. SI-SA-REKS (full line), unscaled CASSCF (dotted line), and CASPT2 (dashed line). The locations of the REKS (full black circle), CASSCF (open black circle), and CASPT2 (open black square) energy minima correspond to avoided crossings (ACs). For the corresponding CI*nt*'s, the corresponding symbols are in red. The insets show the occupation of a stronger occupied active orbital of SSR; the occupation close to 1.0 indicates the COV and/or DIR electronic configuration (see text) which are shaded in blue on the energy profiles; the occupation close to 2.0 indicates the closed-shell CT electronic configuration shaded in brown. (B) Schematic representation of the structure of the S_1 PES driving the photoisomerization of the switch. The photochemical reaction path for the *E*-P,R diastereomer is marked with dashed red (S_1 relaxation) and blue (S_0 relaxation) curves. The angle τ defined in Figure 5C reflects, approximately, the magnitude of the overlap between the π-systems of the indanylidene and pyrrolidone units. The BLA displacement is inverting skeletal double and single bonds along the O═C2′—C3′═C1—C7a═C7—C6═C5—O framework.

Scheme 2. Synthesis of 3 (*p*-HBDI-Like Compound) and Comparison with NAIP Compounds[a]

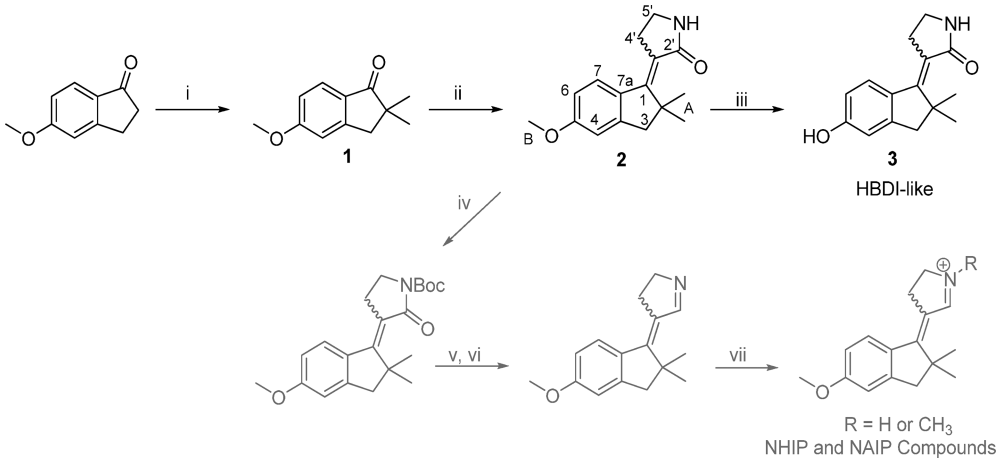

[a]Reagents: (i) MeI, *t*-BuOK, *t*-BuOH, Et_2O; (ii) *N*-Boc-pyrrolidinone, LiHDMS, $BF_3(Et)_2O$, THF, TFA; (iii) BBr_3, DCM; (iv) di-*tert*-butyl dicarbonate, DMAP, TEA, DCM; (v) CH_3MgBr, THF; (vi) TFA, DCM; (vii) MeOTf or HCl, benzene.

only features a significant red shift of the λ_{max} values with respect to the neutral form but also displays solvatochromism. (Notice that the *E*-**3** anion is a racemic mixture of *E*-P,R and *E*-M,S enantiomers while the *Z*-3 anion is a racemic mixture of *Z*-P,R and *Z*-M,S enantiomers).

The computed gas-phase *p*-HBDI-like switch λ_{max} values (also reported in Table 2) fall either relatively close to the observed quantities (SI-SA-REKS) or ca. 5 kcal/mol red-shifted (CASPT2//CASSCF). This may be compared with the NHIP behavior showing gas-phase λ_{max} values significantly, ca. 10 kcal/mol, red-shifted with respect to methanol solution. In NHIP, this is explained by the solvent stabilization of the S_0 charge distribution with respect to the S_1 translocated charge distribution. In fact, the λ_{max} of the close NAIP compound of Scheme 1 (with R = Me) is computed to be 452 nm (*E*) and 449 nm (*Z*) at the CASPT2//CASSCF level[48] and confirmed by a measured gas-phase value of 447 nm for the *Z* isomer, while the observed values in methanol are 377 nm (*E*) and 385 nm (*Z*).[16] The difference between NAIP and *p*-HBDI-like switches can be, in part, explained by the fact that upon vertical excitation NAIP

DOI: 10.1021/jacs.5b10812
J. Am. Chem. Soc. 2016, 138, 9807−9825

Table 2. λ_{max} Value of the *E*-3 and *Z*-3 Neutral and Anionic Forms in Different Solvents

	E-3 (nm)		*Z*-3 (nm)	
solvent (dipole moment)	neutral	anionic[a]	neutral	anionic[a]
water (1.85)	319	348	321	351
methanol (1.70)	320	351	324	359
ethanol (1.69)	320	356	322	360
DMSO (3.96)	320	381	322	386
DMF (3.82)	318	383	319	386
gas phase (computed)		347 (384)[b]		368 (402)[b]
methanol (computed)[c]		375		397

[a]Generated by addition of KOH to the neutral solutions. [b]SI-SA-REKS and CASPT2//CASSCF (in brackets) values. [c]CASPT2//CASSCF/6-31G*/AMBER computations (see last subsection).

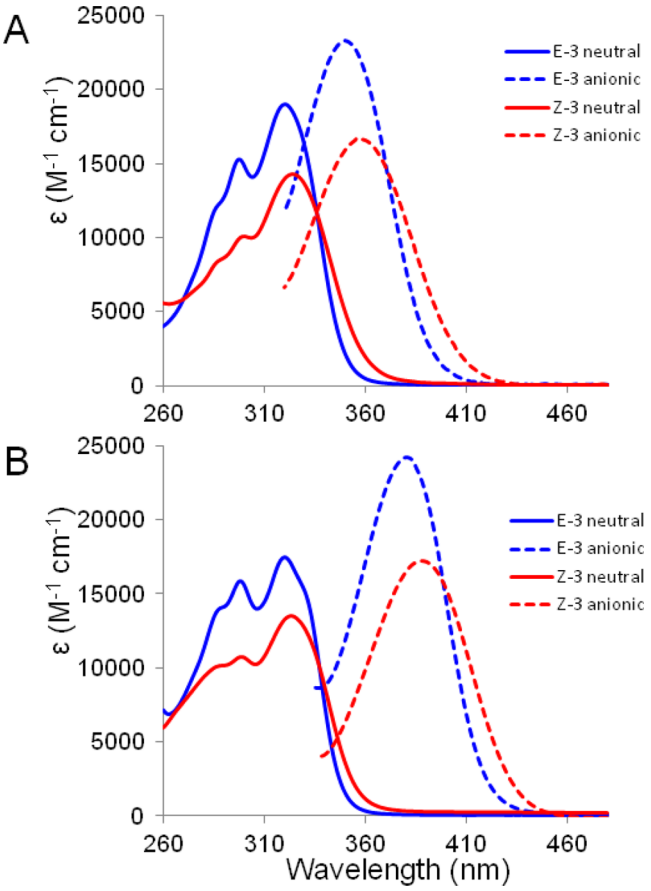

Figure 7. UV–vis absorption spectra of *E*-**3** and *Z*-**3**. The anionic forms are obtained by addition of KOH. (A) Methanol solution. (B) DMSO solution. While the S_0 to S_1 absorption spectrum of the neutral form is structured, that of the anionic form is not. We argue that this could result from the much stronger interaction of the anionic form with polar solvents. The enhanced solute–solvent interaction would damp the observed structure because of enhanced inhomogeneous broadening.

displays a 30% charge transfer between the indanylidene and pyrrolinium moieties[15] while Table 1 shows that our *p*-HBDI-like switch displays a much weaker ca. 10% charge translocation. With a smaller charge translocation occurring upon excitation to S_1, the solvent effect is expected to be of a lesser extent. This is supported by additional TD-DFT calculations performed with and without PCM solvent environment, which show a ca. 10 nm solvent induced blue-shift. As we will discuss below, the use of an explicit solvent model (i.e., a box of methanol molecules described at the molecular mechanics level) predicts, consistently, a 10 and 5 nm solvent induced blue-shift for the *E* and *Z* isomers, respectively.

While it has been reported that the counterions form solvent separated ion pairs in methanol,[16] less separated ion pairs and other factors may be involved in determining the ca. 30 nm red-shift observed in the aprotic DMSO or DMF solvents with respect to methanol. These solvents appear to provide a better stabilization of S_1 with respect to S_0 or, alternatively, a lesser stabilization of the S_0 with respect to S_1 in comparison with protic solvents (e.g., through formation of solvent–solute adducts).

The photoisomerization of **3** was investigated by irradiation in a Pyrex NMR tube at room temperature (ca. 5.0 mg in 0.5 mL of CD_3OD or DMSO-d_6) at three different wavelengths across the absorption bands for each solvent in neutral or anionic form. The isomer composition of the corresponding photostationary states is given in Table 3 and was determined using

Table 3. Analysis of the Photostationary States Composition of the Neutral and Anionic Forms of 3 in Methanol and DMSO, at Different Irradiation Wavelengths

irradiation λ_{max} (nm)	solvent	*E*/*Z* composition (±0.1)	$\varepsilon_E/\varepsilon_Z$[b]	η_{ZtoE}/η_{EtoZ}[c]
Neutral Form				
290	CD_3OD	1/1.40	1/0.68	1/0.95
290	DMSO-d_6	1/1.35	1/0.71	1/0.96
320	CD_3OD	1/1.07	1/0.73	1/0.78
320	DMSO-d_6	1/1.05	1/0.75	1/0.79
360	CD_3OD	1/0.19	1/4.6	1/0.87
360	DMSO-d_6	1/0.21	1/3.1	1/0.66
Anionic Form[a]				
320	CD_3OD	1/1.48	1/0.57	1/0.84
350	DMSO-d_6	1/1.35	1/0.55	1/0.74
350	CD_3OD	1/1.29	1/0.68	1/0.88
380	DMSO-d_6	1/1.32	1/0.69	1/0.91
410	CD_3OD	1/0.11	1/5.3	1/0.58
440	DMSO-d_6	1/0.10	1/5.3	1/0.53

[a]Generated by addition of a drop of 40% NaOD in D_2O. [b]*E*/*Z* ratio of the extinction coefficients ε given in Figure 7. [c]Ratio of the photoisomerization yields calculated as a product of the *E*/*Z* composition of the PSSs by the *E*/*Z* ratio of the extinction coefficients (see text).

^{1}H NMR spectroscopy by computing the area ratio of the signal attributable to H-7. Distinct photostationary states were reached upon irradiation at different wavelengths, demonstrating that it is possible to modulate the isomeric equilibrium in line with the differences in λ_{max} of the two forms.

After irradiation, the resulting mixtures were stored at room temperature in the dark for a few days without displaying a significant change in composition. In line with the ca. 30 kcal/mol S_0 energy barriers computed for double bond isomerization (see Figure 3), the lack of thermal return indicates that the energy barrier for S_0 (i.e., thermal) *Z*/*E* isomerization is high enough to restrain such a process at room temperature. Conversely, upon heating at 100 °C for 24 h in DMSO-d_6, pure *E*-**3** (isolated by flash chromatography) and *E*/*Z* mixtures of **3** in both the neutral and anionic forms yielded an *E*/*Z* ratio of 1/0.1. Under these conditions, no decomposition was observed, confirming the compound chemical stability.

In the absence of thermal isomerization and photodegradation, the relative concentrations [*E*]/[*Z*] of both isomers in the PSSs at a given illumination wavelength are only controlled by the relative excitation probabilities (given by the extinction coefficients ε_E and ε_Z) and the photoisomerization quantum yields (QYs, η_{EtoZ} and η_{ZtoE}) of both isomers at this wavelength. More precisely,

DOI: 10.1021/jacs.5b10812
J. Am. Chem. Soc. 2016, 138, 9807–9825

from the spectra displayed in Figure 7 and the PSS E/Z compositions given in Table 3, we can infer the ratio of QYs of both isomers as $\eta_{ZtoE}/\eta_{EtoZ} = [E]/[Z] \times (\varepsilon_E/\varepsilon_Z)$ also reported in Table 3. This reveals that, for both anion and neutral forms, in MeOH or DMSO, the QYs of both isomers differ by no more than 20% when illuminating at the maximum or high energy side of the absorption spectra. Upon illumination in the red most part of the spectra where the extinction coefficients are much weaker, the QY ratio become inaccurate but remains similar to at most a 50% difference between both isomer QYs. Then, we conclude that the PSS compositions are essentially determined by the relative extinction coefficients of both isomers. This explains why the Z isomer cannot be accumulated as much as the E isomer, since there is no wavelength where Z has a significantly weaker absorption than E.

The absolute photoisomerization quantum yield of the E isomer of the neutral compound in methanol was determined to be 0.19, by HPLC analysis upon irradiation at 315 nm. For the anionic E-**3** compound, a quantum yield of 0.16 was determined by spectrophotometric analysis upon 350 nm irradiation. See the Materials and Methods for details. According to Table 3, the Z isomers have similar or slightly higher (by ∼20%) photoisomerization quantum yields. These values are in the same range as or slightly lower than those of the cationic MeO-NAIP (see Scheme 1: R = R′ = CH_3), which were reported to be 0.34 and 0.19 for the E and Z isomers, respectively,[15] or of E-dMe-MeO-NAIP (see Scheme 1: R = CH_3, R′ = H), reported to be 0.25.[14]

Photoisomerization Dynamics. The computational investigation of the p-HBDI-like switch indicates that the system may undergo light induced isomerization on a sub-picosecond time scale in solution and at room temperature. The synthesis of **3** allowed for an experimental verification of the energy landscape and dynamics summarized in Figure 6B. Accordingly, a methanol solution of pure E-**3** (that is containing <3% of Z-**3**) with an excess of KOH generating the anionic form was investigated by femtosecond transient absorption (TA) spectroscopy in two distinct experiments allowing photoexcitation at two different wavelengths (see the Materials and Methods). First, a 350 nm femtosecond pump, tuned at the S_0 to S_1 absorption maximum, was used to excite the system. Second, a 400 nm pump was used to prepare the system in a different Franck−Condon state minimizing the initial excess of vibrational energy in S_1. Both experiments deliver very similar TA data, and Figure 8 displays an overview of the data obtained upon 350 nm excitation in the form of a 2D map (the same 2D map obtained upon 400 nm excitation is disclosed in Figure S3). Ground state bleach (GSB) is expected as a negative signal (blue coded) at wavelengths where S_0 E-**3** absorbs, and is indeed observed at probing wavelengths shorter than 375 nm. S_1 signatures are observed at early times and are composed of (i) an excited state absorption (ESA) which partially overlaps with the GSB and appears as a positive signal (red coded) in the range 375−440 nm and (ii) a stimulated emission (SE) band appearing as a negative signal (blue to violet) at wavelengths >440 nm. Within the first 1 ps, the early SE and ESA signatures have decayed, to reveal a longer lived (positive, yellow) band centered at 400 nm which further decays and spectrally narrows on the ps time scale to eventually form the relaxed ground state photoproduct absorption (PA) signature, as will be clearly identified below.

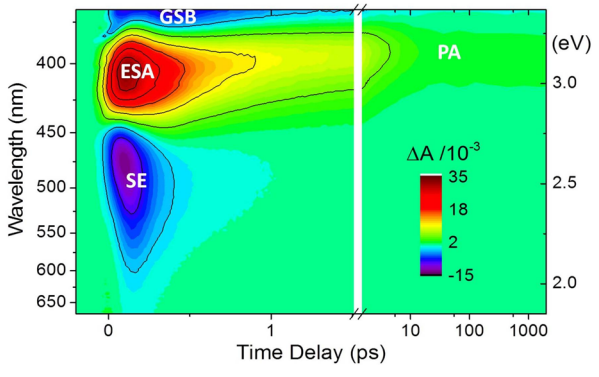

Figure 8. False color 2D map of the TA data (ΔA) measured upon 350 nm excitation of the anionic E-**3** in methanol, as a function of probe wavelength (nm) or energy (eV) and pump−probe time delay (ps).

Figure 9 displays detailed insight into the TA data obtained with E-**3** in methanol upon 350 nm (same data set as in Figure 8) and 400 nm excitations. Parts A and B of Figure 9 compare a selection of TA spectra recorded in both experiments. The various spectral signatures introduced above appear very similar in both experiments, with a somewhat broader ESA band, extending about 20 nm further to the red, when a 350 nm excitation pulse is used, populating higher-lying vibrational levels in the S_1 state. In the 175 fs spectra in both experiments, the SE has already decayed around 450−470 nm, while it has increased at wavelengths λ > 500−550 nm. This indicates spectral relaxation in the S_1 state, attributed to vibrational and possibly very fast polar solvent relaxations.[49] In the 400 fs spectrum, both SE and ESA have decayed significantly while the GSB (λ < 375 nm) remains deep (see in particular Figure 9B). At 1.5 ps, the SE has completely vanished and the GSB has partially recovered, as best seen in the 400 nm pumped experiment where probing wavelengths extend further in the UV (Figure 9B). This spectral shape further evolves on the several ps time scale until a stationary spectrum is observed (Figure 9C), which overlaps with the difference between the Z-**3** and E-**3** steady-state absorption spectra. This is the definitive evidence that the final product is Z-**3** (i.e., a racemic Z-P,R + Z-M,S). Knowing the pure Z-**3** and E-**3** extinction coefficients (Figure 7A), the relative intensity of the final difference spectrum with respect to that of the initial GSB (∼3 mOD at 350 nm, see Figure 9B) allows us to estimate the E to Z photoisomerization quantum yield to be ∼0.22. This estimate is however uncertain due to the overlap of the GSB with the initial strong ESA (i.e., the initial GSB is possibly larger than 3 mOD). Hence, this value should be considered as an upper boundary, in agreement with the reference value of 0.16 obtained by HPLC analysis (see above).

Figure 9D compares a selection of kinetic traces recorded in the SE spectral window with 350 or 400 nm excitation. The traces, which are remarkably similar in both experiments, display a marked (i.e., time-resolved) rise, and the SE signal maximum is observed at a time delay which increases with the wavelength, from ∼100 fs at 463 nm to ∼185 fs at 675 nm (see small vertical arrows in Figure 9D and the more detailed analysis in Figure S4). Whether this behavior reflects a wavelength dependence of the SE signal onset or is due to an overlapping, very short-lived, red to infrared ESA band (as, for instance, observed in the NAIPs[13,17]) is uncertain. In any case, this delayed onset indicates motion/relaxation (or solvation) away from the FC region on the ∼150 fs time scale. Interestingly, in the red-most part of the probing window (see the traces at 675 nm), this motion out of the FC region appears somewhat slower (by ∼50 fs, with an accuracy of ±30 fs) in the 400 nm pump experiment characterized by a minimal excess of vibrational energy. Figure 9E displays the ESA, GSB, and PA kinetics at UV probing wavelengths, a spectral window which is best covered by

DOI: 10.1021/jacs.5b10812
J. Am. Chem. Soc. 2016, 138, 9807−9825

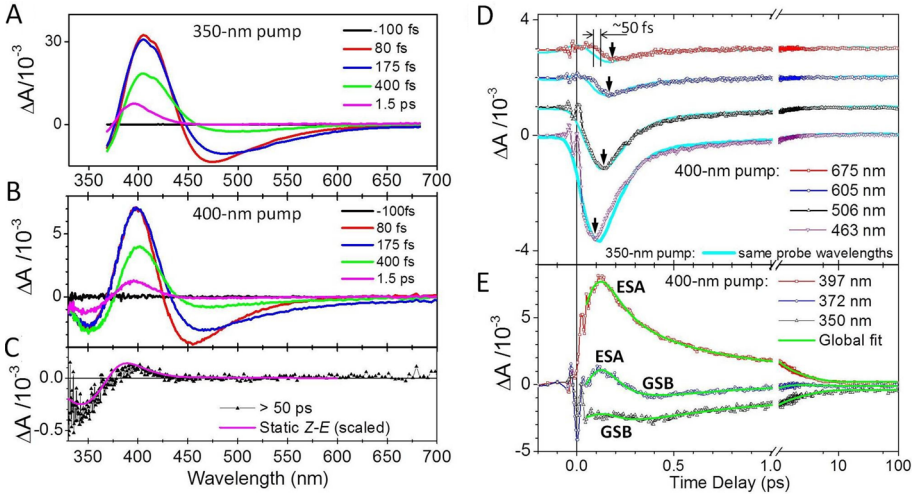

Figure 9. Selection of TA spectra of *E*-**3** in methanol in excess of KOH, obtained upon 350 nm (see panel A) and 400 nm (see panel B) excitation wavelengths. (C) Final (>50 ps) TA spectrum obtained upon 400 nm excitation, overlapped with the difference between static *Z*-**3** and *E*-**3** absorption spectra. (D) Comparison between the kinetic traces observed at a selection of probing wavelengths in the SE band upon 350 and 400 nm excitation. The arrows indicate the maximum of the SE signal amplitude occurring at later times for increasing probing wavelengths. At the 675 nm probing wavelength, there is an indication of a 50 fs larger delay in the SE signal rise when exciting at 400 nm as compared to 350 nm. (E) ESA decay kinetics probed in the UV region upon 400 nm excitation and global fit. The early oscillations observed in the range −50 fs to +50 fs in panels D and E are an artifact resulting from the imperfect cancellation of the intense solvent signal in the 400 nm pumped experiment (see Figures S3 and S4).

the experiment performed with the 400 nm pump, even if imperfect solvent artifact correction causes spurious residual oscillations in the range from −50 to +50 fs. The 396 nm kinetic trace is a simultaneous contribution of the overlapping ESA decay and PA rise and further thermalization. At 372 nm, the decay of the (positive) ESA signal within ∼400 fs reveals the underlying (negative) GSB, while, at 350 nm, the signal remains nearly constant over the first 500 fs, most likely as a result of the compensating time evolutions of both ESA and GSB overlapping at this wavelength.

Quantitative analysis of TA data is commonly done by global fitting, which assumes that spectral (λ) and time (t) variables are separable[50] and is therefore ideally suited to recover exponentially decaying populations characterized by time-independent (i.e., vibrationally relaxed) spectra. In the present case of dynamic spectral shifts, as illustrated above, this assumption becomes questionable and the decay kinetics may deviate, especially at early times, from the multiexponential decay expected from a rate equation modeling of population kinetics. To account for that, we use as a fitting function the sum of a multiexponential decay and of a Gaussian function of standard deviation σ, centered on the time origin, a priori accounting for the instrument response function (see details in the Supporting Information). In the general case, the amplitude of that Gaussian function would account for a nonresolved kinetics (in which case the detected time evolution is indeed that of the IRF). Here, it may also account for the wavelength dependence of the signal onset due, e.g., to dynamic spectral shifts, in which case the parameter σ is no longer solely related to the experimental time resolution. This choice of fitting function is a practical way to significantly improve the quality of the fitting at early times, and therefore also at later times due to the interdependence of the time scales extracted from multiexponential global fitting.

The result of this global fitting of the 350 nm pumped TA data (see details in the Supporting Information, Figure S5) is displayed in Figure 10A in the form of a "Gaussian-associated" spectrum and usual "decay-associated" spectra (DAS). The amplitude of the Gaussian-associated spectrum is low, but still its positive sign at λ > 475 nm and the value of σ = 65 fs (corresponding to a Gaussian fwhm of 2.34 × σ ∼ 150 fs) are accounting for the 150 fs delayed onset of the (negative) SE signal in that wavelength range. Also, its positive and negative extrema around 420 and 380 nm, respectively, are in line with an early blue shift of the (positive) ESA signal on the same time scale, which is close to the experimental time resolution. Then, the 120 fs DAS has the same shape as the SE band at λ > 420 nm, and therefore reveals the decay of the SE signal on this time scale. The positive sign of the same DAS for λ < 420 nm is in line with the decay of

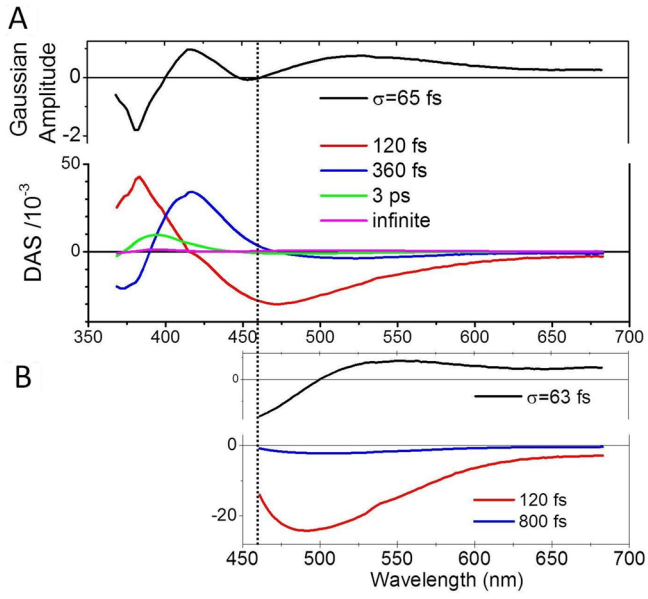

Figure 10. Global analysis of the TA data of *E*-**3** upon 350 nm excitation. (A) Gaussian-associated and Decay-Associated spectra (see details in the Supporting Information) (B) The same analysis performed on the λ > 460 nm portion of the data set enables a more specific characterization of the biexponential decay kinetics of the SE band.

DOI: 10.1021/jacs.5b10812
J. Am. Chem. Soc. 2016, 138, 9807−9825

the short-wavelength portion of the ESA band which overlaps the GSB in that spectral window (Figure 8). This very fast SE and ESA decay is followed by a 400 fs DAS corresponding to the simultaneous recovery of the GSB (λ < 380 nm) and decay of the band peaking at 420 nm. We attribute this DAS to a second excited state decay component. Subsequently, the 3 ps DAS is attributed to ground state spectral relaxation due to further vibrational and solvent relaxation, in line with what was already observed for the NAIP compounds in the same solvent.[16,17] The final "infinite" DAS accounts for the long-lived differential spectrum already discussed in the 400 nm pumped data, Figure 9C.

The same global analysis is done on the 400 nm data, but time delays shorter than 50 fs are disregarded to avoid complications due to spurious solvent artifact in that data set (see details in the Supporting Information). The result of this global fit is illustrated by a selection of wavelengths in Figure 9E. The corresponding DAS (see Figure S6) appear almost identical to Figure 10A, with two excited state decay components of 100 and 430 fs, followed by a 2.5 ps vibrational/solvent cooling in the ground state. This confirms that the excited state dynamics and decay of compound *E*-**3** is weakly affected by the initial excess of vibrational energy and therefore suggests that the vibrational modes optically excited and responsible for the early fast motion out of the FC region are not immediately coupled to the reaction coordinate responsible for the S_1 decay (e.g., torsion around the isomerizing bond). As computationally documented above, this initial motion is dominated by a stretching relaxation (BLA mode), like in other isomerizing systems including NAIPs[51] and rhodopsins.[44] This relaxation unlocks the torsion motion which in turn is induced by the slope of the S_1 potential surface, shown to be rather flat for *E*-**3** (Figure 5).

p-HBDI-Like versus NAIP Isomerization Mechanisms. Figure 11 compares the room temperature kinetic traces recorded upon 400 nm excitation for *E*-**3**, *E*-dMe-MeO-NAIP[14] (see Scheme 1: R = CH_3, R′ = H), and *E*- and *Z*-MeO-NAIP[13] (R = R′ = CH_3) in methanol solutions, at wavelengths representative of the SE decay kinetics. Table 4 compares the excited state lifetimes of the same four compounds. The SE decay kinetics of anionic *E*-**3** (black trace) appears qualitatively similar to that of the cationic *E*-dMe-MeO-NAIP (red trace, see the TA 2D map in Figure S7A).

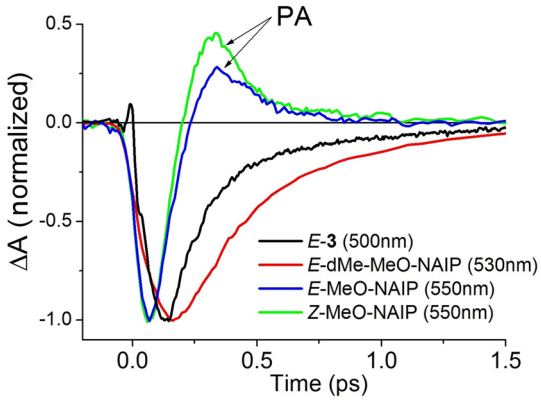

Figure 11. Comparison of the TAS data obtained upon 400 nm excitation for methanol solutions of *E*-**3**, *E*-dMe-MeO-NAIP, and *E*- and *Z*-MeO-NAIP, at a selection of probing wavelengths (in parentheses) representative of the SE decay kinetics of each compound. For both isomers of MeO-NAIP, the rapid SE decay is followed by the impulsive rise of the photoproduct absorption (PA). For the *E*-**3** kinetic trace (black), the very short-lived positive dip around 0 ps is a residual of a solvent-induced signal, not a signature of *E*-**3** dynamics.

For both compounds, the SE signal is seen to increase until 100−160 fs, where it reaches its maximum amplitude. After the maximum, both kinetics are correctly fitted with a biexponential function. For *E*-dMe-MeO-NAIP, the dominating (85%) decay component is 300 fs and the second SE decay time is 0.9 ps, while the ESA decays with a 350 fs decay time, similar to the first component of the SE (see fits in Figure S7B).

In the case of both *E* and *Z* isomers of the cationic MeO-NAIP (R = CH_3, R′ = CH_3), the negative SE signal measured at 550 nm is instead seen to rise instantaneously (i.e., within an experimental time resolution of ∼80 fs in these experiments, see blue and green traces in Figure 11). This is in line with the results of fluorescence up-conversion experiments performed on the *Z* isomer (ref 16) and revealing a biphasic decay with a <40 fs time scale indicative of a dynamic Stokes shift due to fast motion out of the FC on this time scale. Also, the photoreactivity of MeO-NAIP is characterized by the peculiar vibrationally coherent motion (see ref 13) of an S_1 population which decays after about 200 fs, resulting in the impulsive onset of the photoproduct absorption (PA) seen in Figure 11. No such impulsive PA signal is seen in the *E*-**3** nor dMe-MeO-NAIP compounds. In MeO-NAIP, this positive PA signal overlaps and masks any putative longer-lived (negative) SE signal and precludes the biexponential fit analysis of the SE kinetics. However, a second, 300 fs decay component observed in the MeO-NAIP fluorescence emission (ref 16) may well correspond to a subpopulation residing in S_1 somewhat longer than the vibrationally coherent population observed to decay to S_0 already after ∼200 fs.

Altogether, a biphasic SE or fluorescence decay is observed in all compounds, with in addition evidence for a biphasic ESA decay for *E*-**3** with both time constants associated with two distinct spectral signatures. The spectrally broad, red-shifting, and short-lived SE band of *E*-**3** resembles that of MeO-NAIP[13] even if the relaxation dynamics out of the FC region appears slower in *E*-**3**. However, while in MeO-NAIP this broadband, short-lived SE signal is followed by the impulsive onset of a red-detuned photoproduct signature, in *E*-**3** it is followed by the 360−430 fs decay of the 420 nm band, which we attribute to the ESA of S_1 in conformations where SE is instead much weaker (see the small SE amplitude in the 360 fs DAS, Figure 10). This longer excited state lifetime and the lack of impulsive photoproduct are instead similar to the case of dMe-MeO-NAIP, where the SE band is spectrally narrower, does not show such a short 120 fs decay component, and remains detected during the entire S_1 lifetime dominated by a 300−350 fs time constant also characterizing the ESA decay. We therefore conclude that the S_1 dynamics of *E*-**3** can possibly be interpreted in two ways:

(i) Sequential scenario: The motion out of the FC rapidly drives the sytem, within ∼250 fs (∼150 fs spectral shift followed by 120 fs decay), in a distinct configurational subspace of S_1, where the SE and the UV side of the ESA band become much weaker, and only the ESA band centered at 420 nm may be detected. The system subsequently decays to S_0 on the 360−430 fs time scale.

(ii) Parallel scenario: Following the early motion out of the FC region, S_1 decays along two distinct pathways (possibly corresponding to distinct conformations already populated in the ground state), one on the 120 fs time scale, characterized by a dynamically shifting UV ESA and red SE, and a second one on the 360 fs time scale characterized by the 420 nm ESA and weaker SE. The analogy with the

DOI: 10.1021/jacs.5b10812
J. Am. Chem. Soc. 2016, 138, 9807−9825

Table 4. Comparison of the Excited-State Lifetimes (in fs) Measured in Methanol for the Anionic *p*-HBDI-Like upon 350 or 400 nm Excitation and for the Cationic dMe-MeO-NAIP and MeO-NAIP Compounds upon 400 nm Excitation

anionic *p*-HBDI-like *E*-**3** pumped @ 350 nm	anionic *p*-HBDI-like *E*-**3** pumped @ 400 nm	dMe-MeO-NAIP[c] *E*	MeO-NAIP *E* and *Z*
SE[a]: 120 (90%), 800 (10%)	SE[a]: 100 (90%), 600 (10%)	SE: 300 (85%), 900 (15%)	200[d]
ESA[b]: 120 (380 nm), 360 (420 nm)	ESA[b]: 100 (380 nm), 430 (405 nm)	ESA: 350	

[a]A specific global analysis of the SE decay is performed on the *E*-**3** data set spectrally restricted to the SE band (see Figure 10B and Figure S8). [b]Both ESA decay times correspond to distinct ESA bands (absorption maxima given in parentheses); see Figure 10 and Figure SI-6. [c]See data and fit in Figure SI-7. [d]Lifetime of the vibrationally coherent S_1 population; see text.

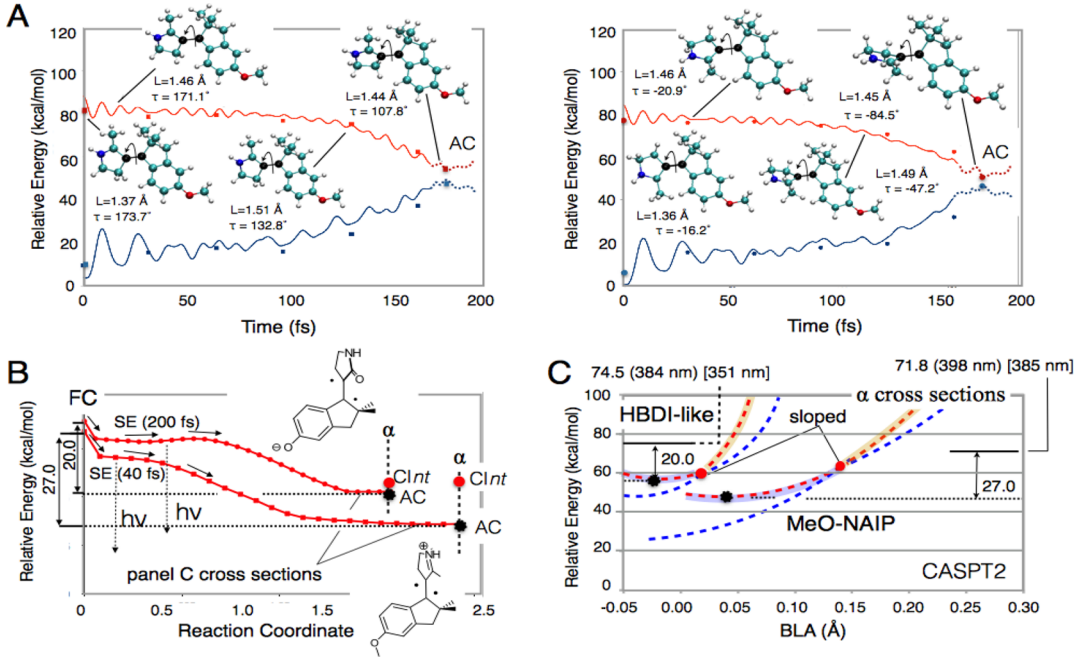

Figure 12. MeO-NHIP FC trajectories and comparison between the *Z* isomer of MeO-NHIP and the *E* isomer of *p*-HBDI-like. (A) Scaled-CASSCF/6-31G* S_1 FC trajectories of *Z*-MeO-NHIP and *E*-MeO-NHIP. The full circles and full squares refer to the single point CASPT2/6-31G* computations performed along the unscaled-CASSCF trajectories and used for scaling the CASSCF energy gaps and time scales (see the Supporting Information for details) given by the full lines. The structures along the trajectories provide information on the main geometrical evolution of the two isomers (parameters in Å and deg). The definitions of the angle τ and bond length *L* are given as insets of Figure 5C. (B) S_1 (red) energy profiles computed along the MEP CASPT2//CASSCF level with a radius of 0.07 and 1.0 Å·(amu)$^{1/2}$ for *p*-HBDI-like and MeO-NHIP, respectively. The dashed vertical segments represent the location of the orthogonal BLA cross sections α in panel C. The energies of the CASPT2 energy minima (AC, black full circle) and CI*nt*'s (red full circle) are also given. (C) Comparison between the S_0 and S_1 energy profiles of the BLA cross sections (see also panel B) for *E*-*p*-HBDI-like and *Z*-MeO-NHIP at the CASPT2 level (dashed line). The locations of the CASPT2 energy minima (AC, black full circle) and CI*nt*'s (red full circle) are also given. Values in parentheses refer to computed values, while values in square brackets refer to experimental values.

case of the NAIP compounds where such a very fast S_1 decay channel results in an impulsive red-detuned photoproduct signature which is not observed here lends credence to the first, sequential scenario.

To rationalize the above comparison between different switches, it is useful to consider the intrinsic structure of their S_1 PESs. This can be done by comparing the three PES elements: the S_1 MEP, the S_1 FC trajectory, and the energy profiles along a BLA scan given in Figure 5A, Figure 5C, and Figure 6A, respectively, for *p*-HBDI-like (*E*-**3** and *Z*-**3**). The corresponding data for MeO-NAIP are instead given in Figure 12. For both switches, the initial motion out of the FC point is initially driven by stretching modes (see initial structures in Figures 5C and 12A which document the *L* expansion) in line with the dashed red line in Figure 6B running, initially, along the "BLA" coordinate. In *p*-HBDI-like, this is followed by slow relaxation along a long energy plateau (this is evident in both the MEP of Figure 5A and the trajectory of Figure 5C) until torsional deformations reach ~40° schematically depicted as the borderline between the brown (CT wave function) and light-blue (COV/DIR wave function) regions (Figure 6B). The same scenario holds for MeO-NAIP switches where the motion out of the FC region is observed both in the SE and ESA signatures[13,17] and it is predicted to occur on a flat but much shorter PES region (see the trajectories in Figure 12A as well as the comparison between the MEP S_1 energy profile in Figure 12B).[16] In fact, MeO-NAIP mimics retinal proteins where a very fast fluorescence relaxation occurs.[52−54]

As evident from the energy profiles in Figure 12B, the differences in the extension and slope of the S_1 plateau indicate that this represents the main cause for the shorter excited-state lifetime of MeO-NAIP (~200 fs in methanol) as compared to that in *p*-HBDI-like (~400 fs for *E*-**3**). The length and slope of the plateau would control the motion toward the decay region. Furthermore, it has been reported that a tiny excited state barrier located along a torsion degree of freedom (which may exist in *E*-**3**) may induce a biexponential decay even if there is only a single decay channel.[55] At the molecular level, the different extension of the S_1 energy plateau can be assigned to the gear conformation of Figure 2 present in the S_0 structure of *E*-**3** (and also found in the *E* form of dMe-MeO-NAIP[14]) which is

DOI: 10.1021/jacs.5b10812
J. Am. Chem. Soc. 2016, 138, 9807−9825

absent both in *Z*-**3** and in the *Z* isomer of MeO-NHIP.[16] Such an arrangement would lend a greater stability of the transient S_1 planar conformations of *E*-**3**. In fact, TA spectroscopy performed on a 55:45 *Z*/*E* mixture of compound **3** upon 400 nm excitation revealed very similar data (see Figure S3), except that the ESA decay appears slightly faster and the relative weight of the slow SE decay component is weaker than for the pure *E* isomer (see Figure S9). This indicates that the "skewed", nonplanar conformation of *Z*-**3** would display a faster S_1 decay due to impossibility of a geared arrangement as in *E*-**3** (see Figure 2B).

Notice that above we have exclusively related the modeled PESs to the relaxation of the excited state signals (SE or ESA). However, the full reactive process would be affected by the detailed topography of the sloped CI*nt*. The fact that measurements were carried out at room temperature and in polar solvent rather than in the gas phase at 0 K sets a limit in the use of the data of Figures 5 and 12 for interpreting the observed time scales. However, the similarity in the S_1 decay, including the biexponential nature of SE or fluorescence kinetics of all compounds, points to a similar kinetic scenario. Consistently, Figure 12C compares the shape of *E*-**3** and *Z*-MeO-NHIP energy profiles in the gas phase in the corresponding AC regions and along the BLA coordinate and reveals that in both cases one has a sloped CI*nt*. Below, using quantum mechanics/molecular mechanics (QM/MM) calculations, we demonstrate that the presence of a polar solvent affects both CI*nt* topologies (see also discussion in the Conclusions section) in a rather predictable and similar way. This similarity is substantially due to the common charge transfer character of the S_1 states of the anionic *p*-HBDI-like and the cationic MeO-NAIP switches. Such character suggests that the solvent (e.g., methanol) may influence the topologies of CI*nt*'s in a similar fashion in the two switches, thus replicating, in solution, what is described already for the gas phase where very similar topographies have been documented.

More specifically, the similarity between the anionic *p*-HBDI-like switch and the cationic MeO-NAIP switch becomes apparent when examining the CT character of their S_1 states. As discussed above, upon light excitation, in the *p*-HBDI-like switch, the anionic center is formally moving from the indanylidene to the pyrrolidone unit, while in NAIPs the cationic center is shifting from the pyrrolinium to the indanyilidene unit. Therefore, both S_1 processes are characterized by a unidirectional transfer of electron density from the indanylidene ring to the pyrrolidone or pyrrolinium rings. This electron density transfer triggers the S_1 BLA change/relaxation that unlocks the central bond torsional motion. A similarity is therefore also expected and found in the twisting mechanism which, in both switches, is dominated by an axial, rather than precessional, rotor twisting with respect to the axis of the isomerizing double bond.[42] This last property is in line with the optimized geometry of the CI*nt*'s and orientation of the BPs which appear very similar for both switches.[16]

The comparison of Tables 1 and 5 provides more quantitative information on the evolution of the charge transfer with respect to the stator and rotor units (i.e., across the reactive double bond) in *p*-HBDI-like and MeO-NHIP switches in the gas phase. As anticipated in the previous section, in S_0, the MeO-NHIP positive charge is localized in the pyrrolinium unit and it gets displaced toward the indanylidene unit upon photoexcitation (see first two entries in Table 5).[15] Similarly, in S_0, the *p*-HBDI-like negative charge is instead partially distributed between the two cyclic units with ca. 60% of the charge

Table 5. Charge Evolution along the Trajectories of Figure 12A[a]

	E-charges		*Z*-charges	
	indanylidene frag.[b]	pyrrolinium frag.[b]	indanylidene frag.[b]	pyrrolinium frag.[b]
S_0 FC	0.34 (0.18)	0.66 (0.82)	0.33 (0.18)	0.67 (0.82)
S_1 FC	0.68 (0.18)	0.32 (0.82)	0.67 (0.18)	0.33 (0.82)
S_1 30 fs	0.58	0.42	0.53	0.47
S_1 60 fs	0.54	0.46	0.57	0.43
S_1 90 fs	0.57	0.43	0.49	0.51
S_1 120 fs	0.52	0.48	0.40	0.60
S_1 150 fs	0.61	0.39	0.29	0.71
S_1 AC	0.05 [0.03]	0.95 [0.97]	0.06	0.94

[a]We set the CT character dominating when the indanylidene fragment has charge ≥0.5 and the COV/DIR character dominating when the indanylidene fragment has charge <0.5. [b]Numbers in parentheses indicate the corresponding values for the REKS optimized structure and the square brackets the values corresponding to the optimized MECI points of Figure 11B.

initially residing in the indanylidene moiety. In this case, a lesser amount of charge (see first two entries in Table 1) gets translocated to the pyrrolidone unit upon light absorption. The difference in the computed evolution of the charge distribution along the S_1 isomerization coordinate of the two switches reflects the different magnitude of these initial changes. In MeO-NHIP, the electron density partially returns to the indanylidene unit and then remains more or less constant up to the AC point where 100% of the positive charge is found on the pyrrolinium unit. This is consistent with the DIR character of the wave function at the S_1 AC minimum discussed above. In the *p*-HBDI-like switch, the initially translocated charge also reverts back but on a slower time scale and magnitude until, as for MeO-NAIP, it suddenly reverts back to a fully DIR wave function more similar to the S_0 than S_1 charge distribution. This occurs, again, at a twisted AC structure. Thus, both *p*-HBDI-like and MeO-NHIP display the charge translocation process leading to a diradical structure at AC. These results are consistent with the assignment of the electronic structures along the S_1 and S_0 states along the α cross sections of Figure 12C (i.e., the AC S_1 minimum has a "light-blue" DIR character, while at the same point the S_0 state has a "brown" CT character).

p-HBDI-Like Isomerization Mechanism in Solution. Figure 13 reports on the FC trajectories computed for *E*-**3** and *Z*-**3** in methanol solution using a QM/MM model (see the Materials and Methods section). The trajectories provide a description of the reactive motion occurring in a solvent glass cavity at 0 K (see Figure 13A). More specifically, the *E*-**3** and *Z*-**3** cavities have been generated via room temperature MD equilibration and are therefore representative of a low temperature solvent glass. The two trajectories describe motion toward the corresponding S_1 minima given in Figure 13B. The S_1 and S_0 energy profiles appear, for both isomers, qualitatively similar to the one obtained in the gas phase. However, when comparing Figure 13C with Figure 5C, the following differences are immediately evident. The first difference is related to the switch λ_{max} values that are slightly blue-shifted with respect to the gas phase (see Table 2). The second difference is related to the time required to reach the S_1 minima that is slightly longer for the switch in solution with respect to the gas phase. The third and more fundamental difference is that the intercepted minima now correspond to degeneracy or near degeneracy regions for *E*-**3** and *Z*-**3**, respectively (i.e., the S_1−S_0 energy gap at the minima

DOI: 10.1021/jacs.5b10812
J. Am. Chem. Soc. 2016, 138, 9807−9825

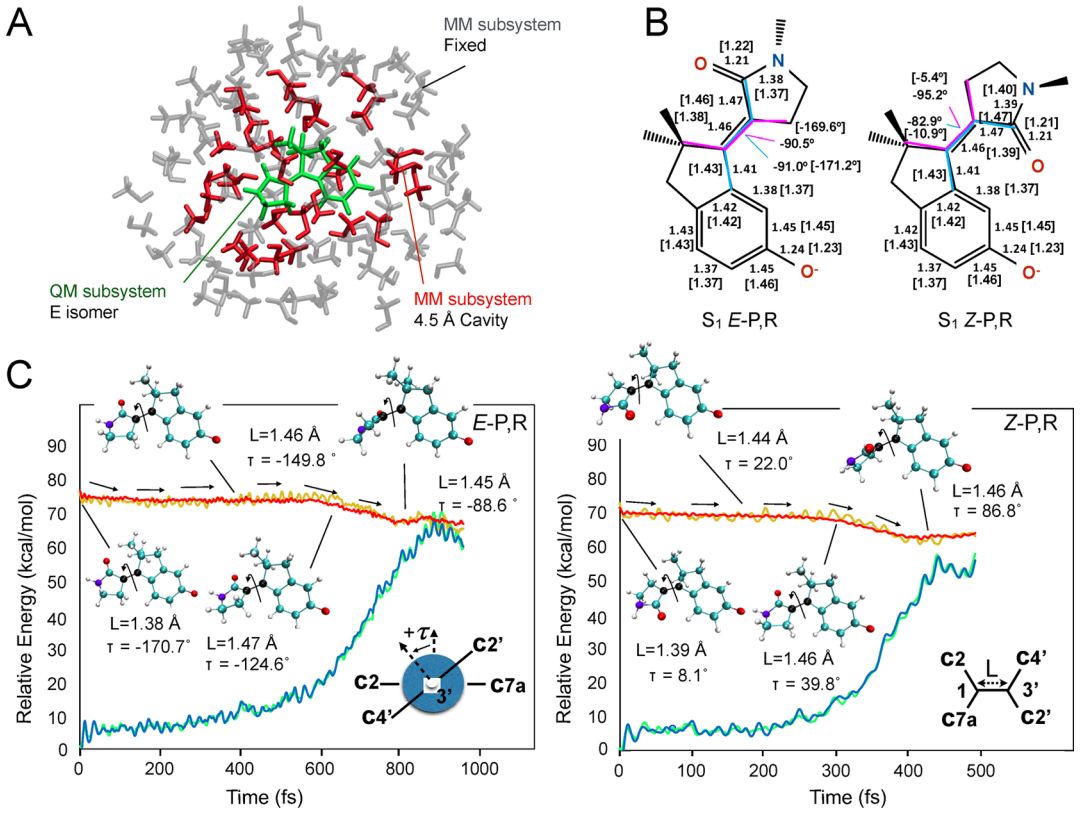

Figure 13. *p*-HBDI-like switch FC trajectories in methanol solution. (A) Structure of the QM/MM model used in the FC trajectory computations in solution. (B) Comparison between the S_0 and S_1 state optimized *E*-P,R and *Z*-P,R structures in methanol solution. The values in square brakets refer to the corresponding S_0 optimized structure. The bond lengths are in Å, and the dihedrals are in deg. (C) Scaled-CASSCF/6-31G* S_1 FC trajectories for *E*-P,R and *Z*-P,R. The red and blue lines represent the S_1 and S_0 scaled-CASSCF energy profiles. The yellow and green lines refer to the S_1 and S_0 energies obtained from single point CASPT2/6-31G* computations performed along the CASSCF trajectories. The structures along the trajectories provide information on the main geometrical evolution of the isomers (parameters in Å and deg). The definitions of the angle τ and bond length *L* are given as insets.

is <4 kcal/mol and therefore much reduced with respect to the >10 kcal/mol of Figure 5C).

When considering the effect of the temperature, the trajectories seem to be consistent with the experimental observations. In fact, as we will also discuss in the Conclusions, the effect of the methanol environment transforms the AC points of the gas-phase switch into CI*nt* (i.e., the sloped CI*nt*'s become peaked), thus explaining the ultrafast decay of the switch to S_0. Also, by definition, FC trajectories describe a motion where the only source of kinetic energy is coming from the acceleration of the molecule along the S_1 PES. Along the flat S_1 PES of **3**, the relaxation must occur via an almost diffusive motion that is expected to be faster in molecules with nonzero initial kinetic energy (i.e., at room temperature). This would explain the longer computed time required to reach the CI*nt* (~800 fs of *E*-**3**) with respect to the observed S_1 lifetime (~400 fs). Also, notice that the flatter S_1 energy surfaces of *p*-HBDI-like switches with respect to MeO-NHIP switches makes the dynamics of the first ones more sensitive to environmental effects. This would explain why the reported MeO-NAIP FC trajectories in methanol solution reach the corresponding CI*nt*'s on a time scale not too different from those of Figure 12A and of ca. 200 fs,[51] in good agreement with experimental findings (Table 4).

CONCLUSIONS

Above, we have reported on the design, preparation, and spectroscopic investigation of a novel *anionic* molecular switch mimicking the electronic structure of the green fluorescent protein chromophore but featuring the same locked framework as *cationic* MeO-NAIP/MeO-NHIP switches. The facile synthesis of **3** has promptly allowed the switch experimental characterization in terms of spectroscopy, photochemistry, and laser-induced ultrafast dynamics. We have shown that the system is photochromic and thermally stable at room temperature and that the anionic form in methanol has *E*-P,R and *Z*-P,R λ_{max} values separated by ca. 10 nm. Furthermore, the photoisomerization of both diastereomers occurs on a sub-picosecond time scale.

The above features have been tentatively rationalized by mapping the intrinsic (i.e., gas-phase) S_0 and S_1 PESs and by running S_1 FC trajectory computations. The effect of the solvent environment has also been investigated by running QM/MM FC trajectory calculations in methanol solution. The results support the schematic mechanism of Figure 14A (also given in Figure 6B) starting with an evolution along a rugged and flat S_1 PES corresponding to a potentially emissive state (i.e., traced by an ~200 fs lived SE signal) of the switch. The corresponding reaction coordinate is initially dominated by a BLA mode and then develops along lower frequency modes including the torsion describing the isomerization of the central double bond until the system reaches a PES region characterized by an AC with ca. 90° twisted structure (i.e., with an orthogonal configuration of the pyrrolidone and indanyilidene rings) and with a DIR electronic character and the negative charge localized on the indanylidene moiety. In the gas phase, a sloped conical intersection (see the inset) is located

DOI: 10.1021/jacs.5b10812
J. Am. Chem. Soc. 2016, 138, 9807−9825

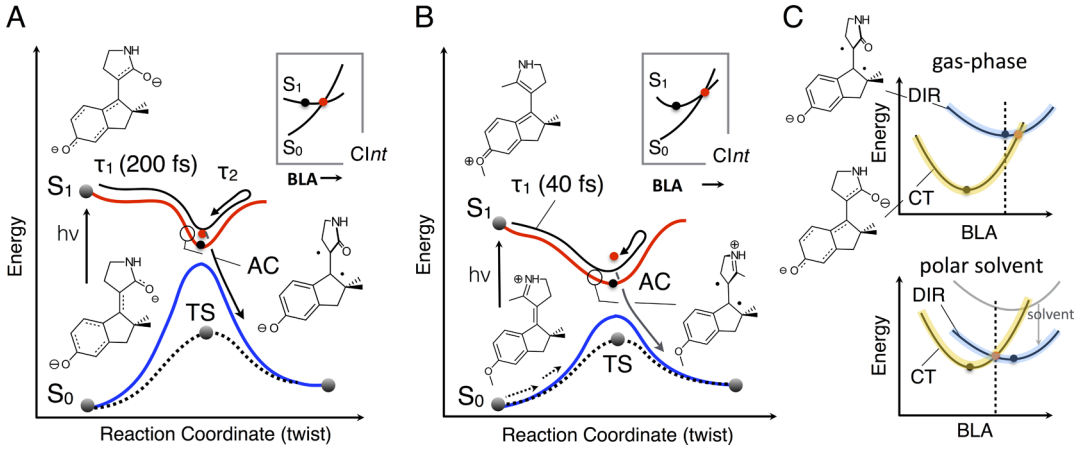

Figure 14. *p*-HBDI-like and MeO-NHIP isomerization mechanisms. (A) Schematic representation of the photochemical reactive trajectories (full black line) for a *p*-HBDI-like switch. A long plateau is entered along the S_1 PES (full red line) restraining the motion toward an AC minimum and a CI*nt* just above it. The CI*nt* has a sloped topography (see inset). The chemical formulas convey the idea that the majority of the S_1 population has initially CT character but along the trajectory a mixed CT/DIR and then almost 100% DIR character develops near the AC minimum (see circled region). (B) The same trajectories for the previously investigated MeO-NHIP switch.[16] In this case, the plateau providing access to the nonadiabatic decay region does not really exist and the progression toward the AC point is faster. The evolution of the electronic character is similar (but of opposite sign) with respect to *p*-HBDI-like. (C) Schematic relationship between the relative stability of the CT and DIR electronic configurations along the BLA coordinate and the topography of the CI*nt* in the gas phase (i.e., for the computed intrinsic *p*-HBDI-like and MeO-NHIP force fields) and in a polar solvent. Notice that along the vertical dashed line the solvent effect turns the S_1 minima into a CI*nt*, as consistently found in Figure 13C. At the same time, a sloped CI*nt* is turned into a peaked CI*nt*.

ca. 1 kcal/mol above the AC point (the same mechanistic picture is obtained when using completely different quantum chemical tools such as DFT and CASPT2//CASSCF methods).

We have also discussed how, remarkably, although compound **3** and the previously investigated MeO-NAIP/MeO-NHIP switches have opposite charges, the photoreactivity is triggered by an electron density translocation occurring in the same direction along the exocyclic reactive double bond. This results in a S_1 dynamics controlled by a qualitatively similar reaction coordinate dominated, sequentially, by BLA and double bond torsion. This is illustrated by the MeO-NHIP mechanistic scheme in Figure 14B where a similar AC and sloped CI*nt* is predicted in the gas phase for both compounds. However, a major difference between the mechanism of Figure 14A and B arises in the FC region where after the stretching relaxation only MeO-NAIP evolves rapidly toward the AC structure with a DIR character. Correspondingly, the lack of an extended S_1 PES would be responsible for a very fast, early spectral relaxation in S_1 in MeO-NAIP, as compared to *E*-**3**.

The reported mapped gas-phase PESs not only inform on the intrinsic S_1 kinetics and reactivity of the two switches but can be useful to estimate the possible effects of the solvent environment allowing to rationalize, on structural bases, the experimental similarity observed between *p*-HBDI-like and NAIPs. Indeed, as illustrated in Figure 14C, a change in the CI*nt* topography from highly sloped to peaked with a consequent disappearance of the AC minima is easily predicted. Such a solvent-induced change would be substantially due to the specific S_0 solvation shell that would create, in a similar way, "effective counterions" surrounding the negatively charged oxygen in *p*-HBDI-like and positively charged nitrogen in NAIP. Assuming that during the measured sub-picosecond S_0 lifetime there is not enough time for the reorganization of the solvation shell, one can predict a stabilization of the DIR electronic structure (where the charges are located close to their S_0 position) with respect to the CT electronic structure. As illustrated in Figure 14C, such stabilization would lead to a change in local topography and, most remarkably, from a "gas-phase" sloped CI*nt* to a "solvated" peaked CI*nt*. Notice that the same effect is predicted to lead to a blue-shift of the λ_{max} with respect to the computed gas-phase quantities.

The qualitative predictions discussed above are found to be consistent with the experimental observations and with the results of our QM/MM FC trajectory computations in methanol solution (see Figure 13C) where (i) the absorption maxima are predicted to be ca. 10 nm blue-shifted with respect to the gas phase, due to the stabilization of the S_0 state with respect to the S_1 state, and (ii) the conical intersection moves at the bottom of the S_1 PES facilitating the decay. Indeed, the difference between the *E*-**3** computed gas-phase λ_{max} value and its corresponding computed λ_{max} values in methanol (as a reference solvent) displays a 10 nm blue-shift due to the stabilization of the S_0 state with respect to the S_1 state. Similarly, for *Z*-MeO-NHIP, one finds even larger blue-shifts of 21 nm when comparing the computed gas-phase λ_{max} (Figure 12C) with the computed quantity in methanol solution (377 nm).[16] In the past, we also reported that the computed S_1 relaxation path for *Z*-MeO-NHIP in methanol intercepted a CI*nt* rather than an AC also consistently with the signatures of coherent motion[17,13] (similar to those reported for bovine rhodopsin and interpreted as the consequences of vibrationally coherent decay at a CI*nt* producing oscillations in the photoproduct PES).[56,57] These data and our FC trajectories in methanol suggest that in polar solvents both *E*-**3** and *Z*-MeO-NHIP intercept peaked CI*nt*'s at the end of their S_1 relaxation paths. These predictions lead us to the expectation that, at room temperature, both compounds may have closer S_1 lifetimes and product appearance times, as actually observed experimentally in methanol.

In conclusion, compound **3** is a new biomimetic molecular switch complementary to NAIP and other retinal chromophore-like switches in terms of charge translocation and S_1 kinetics. Structure **3** can in principle easily be functionalized at the pyrrolidone N atom, thus providing anchor points for linking such a system to a support including a biopolymer (e.g., protein) or a metal surface. A seemingly facile functionalization is also possible for NAIPs but at the level of the indanyilidene unit (see Figure 15). Indeed, N-substitution in the *p*-HBDI-like

DOI: 10.1021/jacs.5b10812
J. Am. Chem. Soc. 2016, 138, 9807−9825

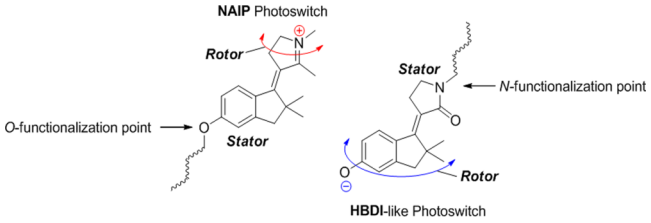

Figure 15. Schematic representation of functionalized complementary NAIP and *p*-HBDI-like photoswitches.

compound and the O-substitution on the indene ring of the NAIPs with clickable alkyl chains are already under scrutiny in our lab. Therefore, *p*-HBDI-like and NAIP photoswitches may realistically form, when combined in a single material, the basis for the production of systems achieving the light-driven rotation of a negatively or positively charged rotor unit respectively leading to light-responsive systems useful in different conditions (e.g., pH, charge, steric hindrance of the rotor, wavelength, etc.).

MATERIALS AND METHODS

Synthesis. All chemicals used were of reagent grade. Yields refer to purified products and are not optimized. Merck silica gel 60 (230−400 mesh) was used for column chromatography. Merck TLC plates and silica gel 60 F_{254} were used for TLC. ^{1}H NMR spectra were recorded at 400 MHz (Bruker DRX-400 AVANCE spectrometer) in the indicated solvents (TMS as internal standard): the values of the chemical shifts are expressed in ppm and the coupling constants (*J*) in Hz. An Agilent 1100 LC/MSD operating with an electrospray source was used in mass spectrometry experiments. The absorption spectra were recorded with a PerkinElmer Lambda 40 in the indicated solvent.

3-(5-Methoxy-2,2-dimethyl-2,3-dihydro-1*H*-inden-1-ylidene)pyrrolidin-2-one (2). To a solution of *N*-Boc-2-pyrrolidinone (6.45 mmol, 1.20 g) dissolved in anhydrous THF (10 mL), a 1 M solution of lithium hexamethyldisilazide (LiHMDS) in anhydrous THF (7.74 mmol, 7.74 mL) was added at −78 °C under a nitrogen atmosphere. After 1 h, a solution of compound **1** (7.74 mmol, 1.47 g) and $BF_3{\cdot}Et_2O$ (7.74 mmol, 976 μL) in anhydrous THF (8 mL) was added dropwise. The reaction mixture was stirred at −78 °C for 3 h. Then, NH_4Cl (s.s.) was added, and the crude was extracted with CH_2Cl_2. The combined organic layers were dried over Na_2SO_4 and concentrated under reduced pressure. The oily residue was dissolved in CH_2Cl_2 (15 mL), and trifluoroacetic acid (1.0 mL) was added. The resulting reaction mixture was stirred at room temperature for 30 min. Then, $NaHCO_3$ (s.s.) was added and the crude was extracted with CH_2Cl_2. The residue was purified by flash chromatography on silica gel (1:1, ethyl acetate/petroleum ether) to obtain compound **2** (1.26 g, 76%) as a pale yellow solid (8:2 mixture of *E*/*Z* isomers). For analytical purposes, *E*-**2** and *Z*-**2** isomers were separated by flash chromatography.

*(E)-3-(5-Methoxy-2,2-dimethyl-2,3-dihydro-1H-inden-1-ylidene)-pyrrolidin-2-one (E-**2**).* ^{1}H NMR (400 MHz, $CDCl_3$): 1.57 (m, 6H, H_A), 2.95 (s, 2H, H_3), 3.19 (t, 2H, *J* = 6.6, $H_{4'}$), 3.48 (t, 2H, *J* = 6.6, $H_{5'}$), 3.84 (s, 3H, H_B), 6.77−6.88 (m, 2H, H_4 and H_6), 7.44 (d, 1H, *J* = 8.4, H_7). ^{13}C NMR (100 MHz, $CDCl_3$): 27.4 (C_A), 32.2 ($C_{4'}$), 39.5 ($C_{5'}$), 45.1 (C_2), 50.9 (C_3), 55.3 (C_B), 109.5 (C_4), 113.2 (C_6), 120.1 ($C_{3'}$), 127.5 (C_7), 133.9 (C_{7a}), 149.6 (C_{3a}), 156.9 (C_1), 160.8 (C_5), 172.4 ($C_{2'}$). NOE experiments showed contacts between $H_{4'}$ (t, δ = 3.19) and H_7 (d, δ = 7.44). MS (ESI): *m*/*z* 280.0 (M + Na^+).

*(Z)-3-(5-Methoxy-2,2-dimethyl-2,3-dihydro-1H-inden-1-ylidene)-pyrrolidin-2-one (Z-**2**).* ^{1}H NMR (400 MHz, $CDCl_3$): 1.31 (m, 6H, H_A), 2.82 (s, 2H, H_3), 3.08 (t, 2H, *J* = 6.6, $H_{4'}$), 3.44 (t, 2H, *J* = 6.7, $H_{5'}$), 3.81 (s, 3H, H_A), 6.69 (s, 1H, H_4), 6.75 (dd, 1H, *J* = 2.4, 8.9, H_6), 8.61 (d, 1H, *J* = 8.9, H_7). ^{13}C NMR (100 MHz, $CDCl_3$): 26.6 (C_A), 28.3 ($C_{4'}$), 39.6 ($C_{5'}$), 47.1 (C_2), 49.3 (C_3), 55.2 (C_B), 108.8 (C_4), 112.3 (C_6), 119.8 ($C_{3'}$), 130.9 (C_{7a}), 131.1 (C_7), 148.4 (C_{3a}), 155.9 (C_1), 160.6 (C_5), 173.0 ($C_{2'}$). NOE experiments showed contacts between $H_{4'}$ (t, δ = 3.08) and H_A (m, δ = 1.31). MS (ESI): *m*/*z* 280.0 (M + Na^+).

3-(5-Hydroxy-2,2-dimethyl-2,3-dihydro-1*H*-inden-1-ylidene)pyrrolidin-2-one (3). To a solution of compound **2** (0.10 g, 0.39 mmol) in dichloromethane (10 mL) cooled to 0 °C was added dropwise a solution (1 M in CH_2Cl_2) of BBr_3 (3.9 mL, 3.9 mmol). The resulting mixture was stirred for 3 h at room temperature. Then, a saturated $NaHCO_3$ solution was added until the gas evolution ceased. The reaction mixture was extracted with dichloromethane, and the organic layer was dried over sodium sulfate and evaporated under reduced pressure. Purification of residue by flash chromatography with petroleum ether-ethyl acetate (1:1) as the eluent gave pure compound **3** (0.90 g, yield 89%) as a pale yellow solid (8:2 mixture of *E*/*Z* isomers). *E*-**3** and *Z*-**3** isomers were separated by flash chromatography using petroleum ether-ethyl acetate (8:2) as the eluent. The fast concentration under reduce pressure at 45 °C of the column fraction containing *E*-**3** provided the pure (>97%) compound which was crystallized from a mixture of CH_2Cl_2/methanol (9:1). Instead, concentration under reduced pressure at 45 °C of the column fraction containing *Z*-**3** provided the *Z*/*E* mixture (55/45) used in the TAS study. For analytical purposes, a pure (>97%) sample of *Z*-**3** was obtained by evaporating the column fractions with a gentle stream of nitrogen.

*(E)-3-(5-Hydroxy-2,2-dimethyl-2,3-dihydro-1H-inden-1-ylidene)-pyrrolidin-2-one (E-**3**).* ^{1}H NMR (400 MHz, CD_3OD): 1.51 (m, 6H, H_A), 2.86 (s, 2H, H_3), 3.12 (t, 2H, *J* = 6.7, $H_{4'}$), 3.42 (t, 2H, *J* = 6.7, $H_{5'}$), 6.68 (s, 1H, H_4), 6.70 (dd, 1H, *J* = 2.2, 8.6, H_6), 7.40 (d, 1H, *J* = 8.6, H_7). ^{1}H NMR (400 MHz, DMSO-d_6): 1.45 (m, 6H, H_A), 2.79 (s, 2H, H_3), 3.00 (t, 2H, *J* = 6.4, $H_{4'}$), 3.27 (t, 2H, overlap with H_2O, $H_{5'}$), 6.60−6.74 (m, 2H, H_4 and H_6), 7.33 (d, 1H, *J* = 8.4, H_7), 7.71 (brs, 1H, OH), 9.70 (br s, 1H, NH). ^{13}C NMR (100 MHz, CD_3OD): 28.0 (C_A), 32.2 ($C_{4'}$), 40.8 ($C_{5'}$), 46.0 (C_2), 51.9 (C_3), 112.3 (C_4), 115.3 (C_6), 121.0 ($C_{3'}$), 129.1 (C_7), 133.9 (C_{7a}), 150.7 (C_{3a}), 158.6 (C_1), 160.4 (C_5), 174.5 ($C_{2'}$). NOE experiments showed contacts between $H_{4'}$ (t, δ = 3.12) and H_7 (d, δ = 7.40). MS (ESI): 266.0 *m*/*z* (M + Na^+).

*(Z)-3-(5-Hydroxy-2,2-dimethyl-2,3-dihydro-1H-inden-1-ylidene)-pyrrolidin-2-one (Z-**3**).* ^{1}H NMR (400 MHz, CD_3OD): 1.30 (m, 6H, H_A), 2.77 (s, 2H, H_3), 3.07 (t, 2H, *J* = 6.6, $H_{4'}$), 3.40 (t, 2H, *J* = 6.6, $H_{5'}$), 6.56 (dd, 1H, *J* = 2.4, 8.7, H_6), 6.60 (s, 1H, H_4), 8.32 (d, 1H, *J* = 8.7, H_7). ^{1}H NMR (400 MHz, DMSO-d_6): 1.22 (m, 6H, H_A), 2.70 (s, 2H, H_3), 2.93 (t, 2H, *J* = 6.6, $H_{4'}$), 3.24 (t, 2H, *J* = 6.5, $H_{5'}$), 6.49 (dd, 1H, *J* = 2.2, 8.7, H_6), 6.55 (s, 2H, H_4), 7.73 (br s, 1H, OH),8.54 (d, 1H, *J* = 8.7, H_7), 9.53 (br s, 1H, NH). ^{13}C NMR (100 MHz, CD_3OD): 27.0 (C_A), 29.4 ($C_{4'}$), 40.9 ($C_{5'}$), 48.3 (C_2), 50.2 (C_3), 111.5 (C_4), 114.3 (C_6), 120.7 ($C_{3'}$), 131.1 (C_{7a}), 132.0 (C_7), 150.0 (C_{3a}), 158.0 (C_1), 159.9 (C_5), 175.1 ($C_{2'}$). NOE experiments showed contacts between $H_{4'}$ (t, δ = 3.07) and H_A (m, δ = 1.30). MS (ESI): 266.0 *m*/*z* (M + Na^+).

Photoisomerization Quantum Yields. Absorption spectra were recorded on a PerkinElmer - Lambda 800 spectrophotometer. The sample was irradiated using a xenon lamp equipped with a monochromator for the selection of the excitation wavelength (315 or 350 nm). A potassium ferrioxalate solution was used as an actinometer to determine the light source intensity at the different excitation wavelengths. The chromatographic analysis was performed using a Waters apparatus equipped with a Lux cellulose 1 column and a UV−vis diode array detector. The protocols followed for the quantum yield measurement of the neutral and anionic forms of *E*-**3** are also reported in refs 58 and 46, respectively.

Transient Absorption Spectroscopy. Transient absorption spectroscopy (TAS) was performed at two distinct excitation wavelengths of 350 nm (at the maximum of the absorption band) and of 400 nm (for minimum excess vibrational energy). The 350 nm pump pulse is produced by a commercial OPA followed by a frequency mixing stage (TOPAS, Light conversion) and pumped by the fundamental 800 nm pulse of an amplified laser system (Amplitude Technologies) operating at 5 kHz. This TA experiment achieves an ∼80 fs time resolution. Another TA experiment is performed with a recently built setup[59] producing a broadband 400 nm pulse. Another amplified Ti:Sa laser system (Amplitude Technologies) is used,

DOI: 10.1021/jacs.5b10812
J. Am. Chem. Soc. 2016, 138, 9807−9825

generating 40 fs, 3 mJ pulses centered at 810 nm with a repetition rate of 1 kHz. In short, nonlinear propagation of about 1 mJ of that fundamental pulse inside a hollow fiber filled in with neon (commercial system by Imperial College Consultants) induces large spectral broadening and yields a red to infrared, sub-7 fs pulse after recompression with a set of chirped mirrors. Type II sum frequency mixing of the sub-7 fs pulse with the fundamental 40 fs pulse yields the 400 nm pulse displayed in Figure S10. This 400 nm pulse is used without any further recompression as a pump beam and provides TA data with sub-30 fs time resolution. In both experiments, the probe pulse is a white light supercontinuum generated in CaF_2 with the 800 nm fundamental pulse (at 5 or 1 kHz, in either setup).

Both pump and probe beams are focused into a 0.2 mm thick quartz flow cell containing the sample in solution. A peristaltic pump is used to circulate the sample so as to refresh it between successive excitation laser shots. TAS is performed on methanol solutions of compound **3** in excess of KOH. Three experiments are performed, on the >97% pure E isomer with (i) 400 nm and (ii) 350 nm excitation wavelength and (iii) on a 55% *Z*/45% *E* mixture of both isomers, with 400 nm excitation wavelength. The sample absorbance at 350 nm is 0.6 over the 0.2 mm thickness of the flow cell in all TAS experiments. Taking into account the spectral overlap between the 400 nm pump laser spectrum and the absorption spectrum of each isomer (see Figure S8), we conclude that, in a mixture of both isomers, the excitation probability of the *Z* isomer is about twice as much as that of the *E* isomer.

All TAS data presented here (see 2D maps in the Supporting Information) are postprocessed in order to compensate for the group velocity dispersion in the probe beam so as to define accurately the time zero (within ±20 fs) at all wavelengths. At very early times, the nonlinear interaction of pump and probe beams in the solvent and cuvette generates a time- and wavelength-dependent signal (see ref 60), sometimes called "coherent artifact". The latter is recorded separately in pure solvent and subtracted to the data recorded on solutions of compound **3**. With the more intense 400 nm pump pulse (see next paragraph), the artifact does not perfectly cancel out, and kinetic traces remain spoiled at very early times by that "solvent" signal. Therefore, the fits of kinetic traces only start after 50 fs.

All experiments are performed within the linear regime of excitation. More precisely, in the 350 nm pumped experiment, the probe beam diameter is ∼60 μm, while the pump is ∼100−120 μm in diameter and 36 nJ in pulse energy (180 μW at 5 kHz repetition rate). With the extinction coefficient of *E*-**3** being ∼23 000/M/cm (see Figure 7A), the Beer−Lambert law predicts that the maximum excitation probability is therefore ∼5%. With the 400 nm pumped experiment, the pump and probe beam diameters are, respectively, ∼250 and ∼140 μm. The column-averaged excitation probabilty is ≤1%, given by the ratio between the early bleach signal at 350 nm, estimated in Figure 9B to be 3−5 mOD (uncertain because of the ESA band partial overlap), and the absorbance of 600 mOD of the sample in the flow cell. This second estimate confirms the ∼5 times higher excitation propobability estimated with the 350 nm pump, since the TA signal is indeed 4−5 times larger in Figure 9A. Finally, since the absorbance of compound *E*-**3** is ∼25 times stronger at 350 nm than at 400 nm, the 400 nm pulse fluence must be ∼5 times larger to achieve 5 times weaker excitation probability, resulting in a much more intense coherent artifact, relative to the compound signal.

Computations. Computational work was performed using the REKS and SI-SA-REKS methods (see ref 37 and references cited therein). The methods employ ensemble density functional theory and are capable of delivering results matching the accuracy of high-level multireference *ab initio* wave function methods, such as MRCISD and XMCQDPT2, when describing ground (REKS) and excited (SI-SA-REKS) state PESs and conical intersections of large molecular systems. The capabilities of the SI-SA-REKS method were demonstrated in direct comparison with the results of the most accurate multireference *ab initio* wave function method, MRCISD, carried out for a wide range of organic and biological chromophores and conical intersections.[61,62]

In the present work, the REKS and SI-SA-REKS (in the following, abbreviated to SSR) methods are employed in connection with the long-range corrected LC-ωPBE[63−65] density functional and the 6-31G* basis set[66] augmented by the diffuse functions on the N and O atoms. The SSR-LC-ωPBE/6-31(+)G* and RE-LC-ωPBE/6-31(+)G* calculations were carried out in the gas phase.

In the ground electronic state, the geometries of all stationary points were located using the RE-LC-ωPBE/6-31(+)G* method. The vertical excitation energies at the optimized S_0 geometries were subsequently calculated using the SSR-LC-ωPBE/6-31(+)G* method (see the FC points in Figure 3). This computational protocol yields accurate vertical excitation energies consistent with correlated methods such as MRCISD+Q, as was demonstrated in previous works,[62,67] Mapping of the ground and excited state PESs along the torsional reaction coordinate was carried out by a relaxed scan along the C2′−C3′−C1−C7a dihedral angle using the SSR-LC-ωPBE/6-31(+)G* method. During the scan, the geometries were optimized for the averaged (i.e., $S_0 + S_1$) state by constraining the C2′−C3′−C1−C7a dihedral angle to specific values incremented through steps of 10°. The energies of the S_0 stationary points obtained in the scan match the respective energies obtained in the ground state RE-LC-ωPBE/6-31(+)G* geometry optimizations within less than 2 kcal/mol.

The MEP and excited state trajectories necessary to investigate the isomerization mechanism are computed at the CASSCF level of theory with a 12 electrons in 11 π-orbitals active space (the nitrogen lone pair is excluded) similar to the active space adopted for other HBDI-like chromophores.[38,39] In order to check for consistency with the SI-SA-REKS level, CASPT2//CASSCF/6-31G* single point computations have been carried out along both the MEPs and the trajectories to reevaluate the energy profiles. As originally done for the NAIP photoswitches, the CASPT2 calculations have been carried out using a three-root state average zero-order CASSCF wave function (with the IPEA = 0 parameter). The SI-SA-REKS level computations have been carried out with the COLOGNE12 suite of programs.[68] The CASSCF and CASPT2 computations have been carried out with MOLCAS 7.8.

The study of the molecular switch in a solvent environment was performed following a procedure presented in Melloni and co-workers[51] and is described here. To construct the model of the switch in a solvent, the ground state optimized chromophore in the gas phase was embedded in the center of a cubic box of size 39.75 × 39.75 × 39.75 $Å^3$ containing methanol. The chromophore was kept frozen, and the solvent system was minimized at the molecular mechanics (MM) level by 1000 conjugate-gradient minimization steps with periodic boundary conditions. The nuclear charges of the chromophore atoms for this purpose were computed using the electrostatic potential fitted method (ESPF) at the CASSCF 6-31G* level of theory using MOLCAS computer software.[69] The minimized solvent system was relaxed using a molecular dynamic simulation while keeping the chromophore fixed. This was done within the isothermal−isobaric NPT ensemble at 1 atm pressure and 298 K temperature. The construction of the solvent box, solvent minimization, and the relaxation were performed using the GROMACS computer package.[70,71] The generalized Amber force field (GAFF) parameters for the chromophore were generated using the ANTECHAMBER software package[72,73] and were used for the molecular mechanics calculations throughout this work. Then, a QM/MM model was defined for the solvent system (see Figure 12). In this model, the chromophore and the solvent are treated at the QM and MM levels, respectively. The solvent molecules located within 4.5 Å of any QM atom were allowed to move during the computations, and the rest was kept frozen. The chromophore was reoptimized in its ground and excited states employing a CASSCF/6-31G*/AMBER protocol with an active space comprised of 12 electrons in 11 orbitals. A Franck−Condon trajectory was also propagated for 1 ps. All the QM/MM calculations were carried out by coupling MOLCAS to the TINKER software package.[74]

■ ASSOCIATED CONTENT

Supporting Information

The Supporting Information is available free of charge on the ACS Publications website at DOI: 10.1021/jacs.5b10812.

DOI: 10.1021/jacs.5b10812
J. Am. Chem. Soc. 2016, 138, 9807−9825

Spectroscopic and computational details and Cartesian coordinates of the computed stationary points and conical intersections (PDF)
Crystallographic structure of compound *E*-**2** (CIF)
Crystallographic structure of compound *E*-**3** (CIF)

AUTHOR INFORMATION

Corresponding Authors

*paomar@oneonline.it
*mike.filatov@gmail.com
*Jeremie.Leonard@ipcms.unistra.fr
*molivuc@bgsu.edu

Author Contributions

¶These authors contributed equally to this work.

Notes

The authors declare no competing financial interest.

ACKNOWLEDGMENTS

This work was supported mainly by the Italian MIUR for funding (PRIN 2010-2011) and, in part, by the National Science Foundation under grant nos. CHE-1152070 and CHE-1151416, the Human Frontier Science Program Organization under grant RGP0049/2012CHE09-56776, and the EU FP7 Marie Curie fellowship PIOF-GA-2012-332233 granted. M.O. is grateful to NSF-XSEDE and Ohio Supercomputer Center for granted computer time. M.F. is grateful to the Korean Ministry of Science for support within the framework of the Brain Pool program. M.G. and J.L. acknowledge support from the Région Alsace (contrat doctoral, # 607-12-C31) and from the French Agence Nationale de la Recherche via the ANR-11-JS04-010-01 "IPQCS" grant, and via the "Investissement d'Avenir" program: Labex NIE ANR-11-LABX-0058_NIE, Labex CSC ANR-10-LABX-0026_CSC, Equipex UNION ANR-10-EQPX-52-01.

REFERENCES

(1) Browne, W. R.; Feringa, B. L. *Nat. Nanotechnol.* **2006**, *1*, 25−35.
(2) Balzani, V.; Credi, A.; Venturi, M. *Chem. Soc. Rev.* **2009**, *38*, 1542−550.
(3) Pollard, M. M.; Klok, M.; Pijper, D.; Feringa, B. L. *Adv. Funct. Mater.* **2007**, *17*, 718−729.
(4) Tahara, R.; Morozumi, T.; Nakamura, H.; Shimomura, M. *J. Phys. Chem. B* **1997**, *101*, 7736−7743.
(5) Collins, G. E.; Choi, L.-S.; Ewing, K. J.; Michelet, V.; Bowen, C. M.; Winkler, J. D. *Chem. Commun.* **1999**, 321−322.
(6) Lemieux, V.; Spantulescu, M. D.; Baldridge, K. K.; Branda, N. R. *Angew. Chem., Int. Ed.* **2008**, *47*, 5034−5037.
(7) Blanco-Lomas, M.; Samanta, S.; Campos, P. J.; Woolley, G. A.; Sampedro, D. *J. Am. Chem. Soc.* **2012**, *134*, 6960−6963.
(8) Kienzler, M. a.; Reiner, A.; Trautman, E.; Yoo, S.; Trauner, D.; Isacoff, E. Y. *J. Am. Chem. Soc.* **2013**, *135*, 17683−17686.
(9) Quandt, G.; Höfner, G.; Pabel, J.; Dine, J.; Eder, M.; Wanner, K. T. *J. Med. Chem.* **2014**, *57*, 6809−6821.
(10) Greb, L.; Lehn, J. *J. Am. Chem. Soc.* **2014**, *136*, 13114−13117.
(11) Guo, X.; Zhou, J.; Siegler, M. a.; Bragg, A. E.; Katz, H. E. *Angew. Chem., Int. Ed.* **2015**, *54*, 4782−4786.
(12) Zanirato, V.; Pollini, G. P.; De Risi, C.; Valente, F.; Melloni, A.; Fusi, S.; Barbetti, J.; Olivucci, M. *Tetrahedron* **2007**, *63*, 4975−4982.
(13) Léonard, J.; Schapiro, I.; Briand, J.; Fusi, S.; Paccani, R. R.; Olivucci, M.; Haacke, S. *Chem. - Eur. J.* **2012**, *18*, 15296−15304.
(14) Dunkelberger, A. D.; Kieda, R. D.; Shin, J. Y.; Rossi Paccani, R.; Fusi, S.; Olivucci, M.; Fleming Crim, F. *J. Phys. Chem. A* **2012**, *116*, 3527−3533.
(15) Lumento, F.; Zanirato, V.; Fusi, S.; Busi, E.; Latterini, L.; Elisei, F.; Sinicropi, A.; Andruniów, T.; Ferré, N.; Basosi, R.; Olivucci, M. *Angew. Chem., Int. Ed.* **2007**, *46*, 414−420.
(16) Sinicropi, A.; Martin, E.; Ryazantsev, M.; Helbing, J.; Briand, J.; Sharma, D.; Léonard, J.; Haacke, S.; Cannizzo, A.; Chergui, M.; Zanirato, V.; Fusi, S.; Santoro, F.; Basosi, R.; Ferré, N.; Olivucci, M. *Proc. Natl. Acad. Sci. U. S. A.* **2008**, *105*, 17642−17647.
(17) Briand, J.; Braem, O.; Rehault, J.; Leonard, J.; Cannizzo, A.; Chergui, M.; Zanirato, V.; Olivucci, M.; Helbing, J.; Haacke, S. *Phys. Chem. Chem. Phys.* **2010**, *12*, 3178−3187.
(18) Léonard, J.; Briand, J.; Fusi, S.; Zanirato, V.; Olivucci, M.; Haacke, S. *New J. Phys.* **2013**, *15*, 105022.
(19) Mayer, G.; Hechel, A. *Angew. Chem., Int. Ed.* **2006**, *45*, 4900−4921.
(20) Zhang, J. L.; Zhong, J. Q.; Lin, J. D.; Hu, W. P.; Wu, K.; Xu, G. Q.; Wee, A. T. S.; Chen, W. *Chem. Soc. Rev.* **2015**, *44*, 2998−3022.
(21) Zimmer, M. *Chem. Rev.* **2002**, *102*, 759−781.
(22) Subach, F. V.; Verkhusha, V. V. *Chem. Rev.* **2012**, *112*, 4308−4327.
(23) Baldridge, A.; Solntsev, K. M.; Song, C.; Tanioka, T.; Kowalik, J.; Hardcastle, K.; Tolbert, L. M. *Chem. Commun.* **2010**, *46*, 5686−5688.
(24) Stavrov, S. S.; Solntsev, K. M.; Tolbert, L. M.; Huppert, D. *J. Am. Chem. Soc.* **2006**, *128*, 1540−1546.
(25) Follenius-Wund, A.; Bourotte, M.; Schmitt, M.; Iyice, F.; Lami, H.; Bourguignon, J.-J.; Haiech, J.; Pigault, C. *Biophys. J.* **2003**, *85*, 1839−1850.
(26) Voityuk, A.; Michel-Beyerle, M.-E.; Rösch, N. *Chem. Phys. Lett.* **1998**, *296*, 269−276.
(27) Niwa, H.; Inouye, S.; Hirano, T.; Matsuno, T.; Kojima, S.; Kubota, M.; Ohashi, M.; Tsuji, F. I. *Proc. Natl. Acad. Sci. U. S. A.* **1996**, *93*, 13617−13622.
(28) Dickson, R. M.; Cubitt, a B.; Tsien, R. Y.; Moerner, W. E. *Nature* **1997**, *388*, 355−358.
(29) Kummer, A. D.; Kompa, C.; Niwa, H.; Hirano, T.; Kojima, S.; Michel-Beyerle, M. E. *J. Phys. Chem. B* **2002**, *106*, 7554−7559.
(30) Olsen, S.; Lamothe, K.; Martínez, T. J. *J. Am. Chem. Soc.* **2010**, *132*, 1192−1193.
(31) Weber, W.; Helms, V.; McCammon, J. a; Langhoff, P. W. *Proc. Natl. Acad. Sci. U. S. A.* **1999**, *96*, 6177−6182.
(32) Moeyaert, B.; Nguyen Bich, N.; De Zitter, E.; Rocha, S.; Clays, K.; Mizuno, H.; Van Meervelt, L.; Hofkens, J.; Dedecker, P. *ACS Nano* **2014**, *8* (2), 1664−1673.
(33) Blanco-Lomas, M.; Campos, P. J.; Sampedro, D. *Org. Lett.* **2012**, *14*, 4334−4337.
(34) Martínez-López, D.; Yu, M.-L.; García-Iriepa, C.; Campos, P. J.; Frutos, L. M.; Golen, J. A.; Rasapalli, S.; Sampedro, D. *J. Org. Chem.* **2015**, *80*, 3929−3939.
(35) Toker, Y.; Rahbek, D. B.; Klærke, B.; Bochenkova, A. V.; Andersen, L. H. *Phys. Rev. Lett.* **2012**, *109*, 128101.
(36) Gromov, E. V.; Burghardt, I.; Köppel, H.; Cederbaum, L. S. *J. Am. Chem. Soc.* **2007**, *129*, 6798−6806.
(37) Filatov, M. *WIREs Comput. Mol. Sci.* **2015**, *5*, 146−167.
(38) Atchity, G. J.; Xantheas, S. S.; Ruedenberg, K. *J. Chem. Phys.* **1991**, *95*, 1862−1876.
(39) Sellner, B.; Barbatti, M.; Lischka, H. *J. Chem. Phys.* **2009**, *131*, 024312.
(40) Bernardi, F.; Olivucci, M.; Robb, M. A. *Chem. Soc. Rev.* **1996**, *25*, 321−328.
(41) Migani, A.; Olivucci, M. In *Conical Intersections: Electronic Structure, Dynamics and Spectroscopy*; Domcke, W., Yarkony, D. R., Köppel, H., Eds.; Advanced Series in Physical Chemistry; World Scientific: Singapore, 2004; Vol. *15*, pp 271−322.
(42) Filatov, M.; Olivucci, M. *J. Org. Chem.* **2014**, *79*, 3587−3600.
(43) Huix-Rotllant, M.; Filatov, M.; Gozem, S.; Schapiro, I.; Olivucci, M.; Ferré, N. *J. Chem. Theory Comput.* **2013**, *9*, 3917−3932.
(44) Frutos, L. M.; Andruniów, T.; Santoro, F.; Ferré, N.; Olivucci, M. *Proc. Natl. Acad. Sci. U. S. A.* **2007**, *104*, 7764−7769.

DOI: 10.1021/jacs.5b10812
J. Am. Chem. Soc. 2016, 138, 9807−9825

(45) Zilberg, S.; Haas, Y. *Photochem. Photobiol. Sci.* **2003**, *2*, 1256−1263.
(46) Rossi Paccani, R.; Donati, D.; Fusi, S.; Latterini, L.; Farina, G.; Zanirato, V.; Olivucci, M. *J. Org. Chem.* **2012**, *77*, 1738−1748.
(47) Dong, J.; Solntsev, K. M.; Tolbert, L. M. *J. Am. Chem. Soc.* **2006**, *128*, 12038−1239.
(48) Pieri, E. Force Fields and non-Adiabatic Dinamics of Biomimetic Molecular Rotors. MSc Thesis, Università degli Studi di Siena, Italy, 2014.
(49) Horng, M. L.; Gardecki, J. A.; Papazyan, A.; Maroncelli, M. *J. Phys. Chem.* **1995**, *99*, 17311−17337.
(50) Van Stokkum, I. H. M.; Larsen, D. S.; Van Grondelle, R. *Biochim. Biophys. Acta, Bioenerg.* **2004**, *1657*, 82−104.
(51) Melloni, A.; Rossi Paccani, R.; Donati, D.; Zanirato, V.; Sinicropi, A.; Parisi, M. L.; Martin, E.; Ryazantsev, M.; Ding, W. J.; Frutos, L. M.; Basosi, R.; Fusi, S.; Latterini, L.; Ferré, N.; Olivucci, M. *J. Am. Chem. Soc.* **2010**, *132*, 9310−9319.
(52) Kandori, H.; Furutani, Y.; Nishimura, S.; Shichida, Y.; Chosrowjan, H.; Shibata, Y.; Mataga, N. *Chem. Phys. Lett.* **2001**, *334*, 271−276.
(53) Kochendoerfer, G. G.; Mathies, R. A. *J. Phys. Chem.* **1996**, *100*, 14526−14532.
(54) Schmidt, B.; Sobotta, C.; Heinz, B.; Laimgruber, S.; Braun, M.; Gilch, P. *Biochim. Biophys. Acta, Bioenerg.* **2005**, *1706*, 165−173.
(55) Olivucci, M.; Lami, A.; Santoro, F. *Angew. Chem., Int. Ed.* **2005**, *44*, 5118−5121.
(56) Polli, D.; Altoe, P.; Weingart, O.; Spillane, K. M.; Manzoni, C.; Brida, D.; Tomasello, G.; Orlandi, G.; Kukura, P.; Mathies, R. A.; Garavelli, M.; Cerullo, G. *Nature* **2010**, *467*, 440−443.
(57) Wang, Q.; Schoenlein, R. W.; Peteanu, L. A.; Mathies, R. A.; Shank, C. V. *Science* **1994**, *266*, 422−424.
(58) Sampedro, D.; Migani, A.; Pepi, A.; Busi, E.; Basosi, R.; Latterini, L.; Elisei, F.; Fusi, S.; Ponticelli, F.; Zanirato, V.; Olivucci, M. *J. Am. Chem. Soc.* **2004**, *126*, 9349−9359.
(59) Gueye, M.; Nillon, J.; Crégut, O.; Léonard, J. *Rev. Sci. Inst.* **2016**, under review.
(60) Kovalenko, S.; Dobryakov, A.; Ruthmann, J.; Ernsting, N. *Phys. Rev. A: At., Mol., Opt. Phys.* **1999**, *59*, 2369−2384.
(61) Filatov, M. *J. Chem. Theory Comput.* **2013**, *9*, 4526−4541.
(62) Nikiforov, A.; Gamez, J. A.; Thiel, W.; Huix-Rotllant, M.; Filatov, M. *J. Chem. Phys.* **2014**, *141*, 124122.
(63) Vydrov, O. A.; Heyd, J.; Krukau, A.; Scuseria, G. E. *J. Chem. Phys.* **2006**, *125*, 074106.
(64) Vydrov, O. A.; Scuseria, G. E. *J. Chem. Phys.* **2006**, *125*, 234109.
(65) Vydrov, O. A.; Scuseria, G. E.; Perdew, J. P. *J. Chem. Phys.* **2007**, *126*, 154109.
(66) Krishnan, R.; Binkley, J. S.; Seeger, R.; Pople, J. A. *J. Chem. Phys.* **1980**, *72*, 650−654.
(67) Filatov, M.; Huix-Rotllant, M. *J. Chem. Phys.* **2014**, *141*, 024112.
(68) Kraka, E.; Filatov, M.; Zou, W.; Gräfenstein, H.; Izotov, D.; Gauss, J.; He, Y.; Wu, A.; Polo, V.; Olsson, L.; Konkoli, Z.; He, Z.; Cremer, D. *COLOGNE2012*; Southern Methodist University: Dallas, TX, 2012.
(69) Aquilante, F.; De Vico, L.; Ferré, N.; Ghigo, G.; Malmqvist, P.-Å.; Neogrády, P.; Pedersen, T. B.; Pitoňák, M.; Reiher, M.; Roos, B. O.; Serrano-Andrés, L.; Urban, M.; Veryazov, V.; Lindh, R. *J. Comput. Chem.* **2010**, *31*, 224−247.
(70) Lindahl, E.; Hess, B.; van der Spoel, D. *J. Mol. Model.* **2001**, *7*, 306−317.
(71) Berendsen, H. J. C.; van der Spoel, D.; van Drunen, R. *Comput. Phys. Commun.* **1995**, *91*, 43−56.
(72) Wang, J.; Wang, W.; Kollman, P. A.; Case, D. A. *J. Mol. Graphics Modell.* **2006**, *25*, 247−260.
(73) Wang, J.; Wolf, R. M.; Caldwell, J. W.; Kollman, P. A.; Case, D. A. *J. Comput. Chem.* **2004**, *25*, 1157−1174.
(74) Ponder, J. W.; Richards, F. M. *J. Comput. Chem.* **1987**, *8*, 1016−1024.
(75) Liu, X. Y.; Chang, X. P.; Xia, S. H.; Cui, G.; Thiel, W. *J. Chem. Theory. Comput.* **2016**, *12*, 753−764.
(76) Hsu, Y. H.; Chen, Y. A.; Tseng, H. W.; Zhang, Z.; Shen, J. Y.; Chuang, W. T.; Lin, T. C.; Lee, C. S.; Hung, W. Y.; Hong, B. C.; Liu, S. H.; Chou, P. T. *J. Am. Chem. Soc.* **2014**, *136*, 11805−11812.

NOTE ADDED IN PROOF

At the reviewing stage a computational work[75] by Thiel and coworkers was published on-line. The work describes a 5-(4-*para*-hydroxybenzylidene)-2,3-dimethyl-3,5-dihydro-4*H*-imidazol-4-one (*p*-LHBDI) molecular switch more directly related to the GFP fluorophore than our *p*-HBDI-like switch. However, the paper only concerns the neutral form of the switch (not the ionic form) and focuses on the *o*-LHBDI regioisomer. The synthesis of *p*-LHBDI was reported earlier[76] and is different from the one reported here for *p*-HBDI-like. On the other hand, we note that the spectroscopic characterization of both the neutral and anion forms of *o*-LHBDI[76] in ethanol and *p*-HBDI-like in methanol show similar absorption properties but a longer excited state lifetime of the *o*-LHBDI anion.

DOI: 10.1021/jacs.5b10812
J. Am. Chem. Soc. 2016, 138, 9807−9825